RUPRECHT-KARLS-UNIVERSITÄT HEIDELBERG

Florian Staier

High resolution 3D microscopic measurements with micro axial tomography

Diploma thesis

KIRCHHOFF-INSTITUT FÜR PHYSIK

Faculty of Physics and Astronomy

University of Heidelberg

Diploma thesis in Physics

submitted by

Florian Staier

born in Göttingen

2005

High resolution 3D microscopic measurements with micro axial tomography

———

This diploma thesis has been carried out by Florian Staier at the
Kirchhoff-Institute for Physics
under the supervision of
Prof. Dr. Dr. Christoph Cremer

High resolution 3D microscopic measurements with micro axial tomography

Micro axial tomography is a challenging technique in microscopy which improves qualitative and quantitative imaging especially in cytogenetic applications by means of defined sample rotation under the microscope objective. The advantage of tomography in microscopy is an effective improvement of resolution in the direction of the optical axis which is usually about three times worse than lateral resolution. 3d distances can be measured with the precision of isotropic resolution.
A newly developed tomographic device which holds the biological specimen attached to the outside of a glass fiber and rotates it with a small computer conrolled stepper motor was used for measurements.
The usability and the precision of the system is shown in a variety of experiments including distance measurements with beads as well as acquisition and analysis of HeLa cells and mouse embryos.

Hochauflösende 3D Mikroskopie mit dem Mikroaxialtomographen

Mikroaxialtomographie ist eine anspruchsvolle Technik der Mikroskopie, welche die qualitative und quantitative Bildaufnahme besonders bei zytogenetischen Anwendungen durch präzise Probenrotation unter dem Mikroskop verbessert. Vorteil der Tomographie in der Mikroskopie ist eine effektive Verbesserung der Auflösung in der Richtung der optischen Achse, welche normalerweise um den Faktor drei schlechter ist als die laterale Auflösung. 3D Distanzen könen mit der Präzision isotroper Auflösung gemessen werden.
Ein neu entwickelter Tomograph, bei dem sich die biologischen Präparate auf der Außenseite einer computer gesteuert drehbaren Glasfaser befinden, wurde erstmals für Messungen verwendet.
Die Benutzbarkeit und Präzision des Systems wird an Hand einer Vielzahl von Experimenten, einschließlich Distanzmessungen an Beads sowie der Aufnahme und Analyse von HeLa Zellen und Maus Embryos gezeigt.

Contents

List of Figures

1 Introduction

Many discoveries in modern biology are based on the possibility to resolve finer and finer details of structures under investigation. The methods of light microscopy are very well suited for the study of biology at a moderate level of detail. In contrast to other methods like electron microscopy, light microscopy enables the investigation of samples in a well preserved and often even living condition.

Another major advantage of biological light microscopy in comparison to other methods is the possibility of target-specific labeling. By using fluorescent probes (dye molecules) attached to the biologic targets it is possible to determine the spatial distribution of the molecules of interest in the biological specimen [Slavik96]. This development drastically improved the information content of light microscopic images. Using different fluorescent dyes attached to different target molecules, many biologically important questions could be answered by co-localization studies [Manders93]. In addition, using attached GFP mutants, it has recently become possible to genetically modify organisms in such a way that specific cellular proteins intrinsically fluoresce [Patterson97]. All of these developments led to a renaissance of light microscopy.

However, the resolution of a light microscope is limited. In a standard epifluorescent widefield microscope the lowest distance at which two objects can be separated is estimated to be above 230 nm lateral and 540 nm axial. Caused by the principles of microscopic imaging the axial resolution is always about three fold worse than the lateral resolution with all disadvantages for biological studies, e.g. 3d distance or co-localization measurements. The problem of low or missing axial resolution is known from different imaging technics, e.g. x-ray or electron microscopy. As an analog to computed tomography in x-ray diagnosis and electron microscopic tomography the idea of microscopic tomography was born in the 1970s.

The first system that allowed tilting of the specimen in a microscope was constructed by [Skaer75], who rotated the whole microscope slide with the objects of interest. Therefore, the tilting range yielding good optical quality was relatively low (up to $\pm 15^{\circ}$).

In another device the slide was omitted completely and the objects (mostly cells or cell nuclei) were placed into a glass capillary that could be rotated up to 360° [Bradl92] [Bradl94]. However, the application of the capillary revealed some disadvantages. The sample had to be prepared in suspension and sucked into the capillary. This constraint could not be easily adapted to any labeling technique, for in-

stance, fluorescence in situ hybridization (FisH) of specific chromosome regions. Moreover, the suspension had to fulfill additional optical conditions. Because the capillary brought another curved glass surface into the light path, appropriate immersion fluids inside and outside the capillary were necessary to carefully match the refractive index of the glass.

Unfortunately, the conditions of specimen preparation and immersion fluids were most often contradictory. Therefore, the capillary has been replaced by a glass fiber on which the objects can be fixed [Bradl96a][Bradl96b] so that a standard coverglass can be placed between the objective lens and the observed objects to obtain better imaging properties. A large tilting range (up to 360°, depending on the object size) can be preserved also for high numerical aperture (NA) oil immersion objectives that have a very short working distance of typically 190 μm. Within this tilting range angular series of images, in which the same object structures are viewed with the poor axial and the best lateral resolution, can be acquired.

Finally a new automated device was developed which was able to rotate objects attached to the outside of a small glass fiber with a small stepper motor attached to a computer. This device is specially designed for precise rotation of the glass fiber with low lateral and axial movement during tilting.

The aim of this thesis was to do first measurements with the newly designed tomograph to show the usability and precision of the system. Therefore a surface treatment procedure to attach beads as well as biological specimens to the fiber, which is easy and fast enough to be handled as routine work in a biological lab, had do be developed. Measurements with fluorescent nanoparticles (beads) were used to show the precision of the instrument as well as the improvement in resolution gained by tomography. As a second part the tomographic acquisition of biological specimen with different sizes and structure as well as image analysis, e.g. deconvolution was done in collaboration with biologists at the Jackson Lab, Bar Harbor. Therefore HeLa cells and mouse embryos were stained, acquired with the tomograph and the resulting image stacks were analyzed with different state of the art software packages.

2 Biological background

2.1 The cell

Present-day living cells are classified as prokaryotic (bacteria and their close relatives) or eukaryotic. Although they have a relatively simple structure, prokaryotic cells are biochemically versatile and diverse - for example, all of the major metabolic pathways can be found in bacteria, including the three principal energy-yielding processes of glycolysis, respiration, and photosynthesis. Eukaryotic cells are larger and more complex than prokaryotic cells and contain more DNA, together with components that allow this DNA to be handled in elaborate ways. The DNA of the eukaryotic cell is enclosed in a membrane-bound nucleus, while the cytoplasm contains many other membrane-bound organelles, including mitochondria, which carry out the oxidation of food molecules, and, in plant cells, chloroplasts, which carry out photosynthesis. Mitochondria and chloroplasts are almost certainly the descendants of earlier prokaryotic cells that established themselves as internal symbionts of a larger anaerobic cell. Eukaryotic cells are also unique in containing a cytoskeleton of protein filaments that helps organize the cytoplasm and provides the machinery for movement [Alberts98].

It only takes one biological cell to create an organism. In fact, there are countless species of single celled organisms, and indeed multi-cellular organisms like ourselves. A single cell is able to keep itself functional by owning a series of "bio molecular machines" known as organelles. The following list looks at some of these organelles and other characteristics typical of a fully functioning cell.

- **Mitochondrion** An important cell organelle working as the cell's power supply
- **Cytoplasm** A fluid surrounding the contents of a cell
- **Golgi Apparatus** The processing area for the creation of glycoprotein
- **Endoplasmic Reticulum** An important organelle heavily involved in protein synthesis.
- **Vesicles** Packages of substances that are to be used in the cell or secreted by it.

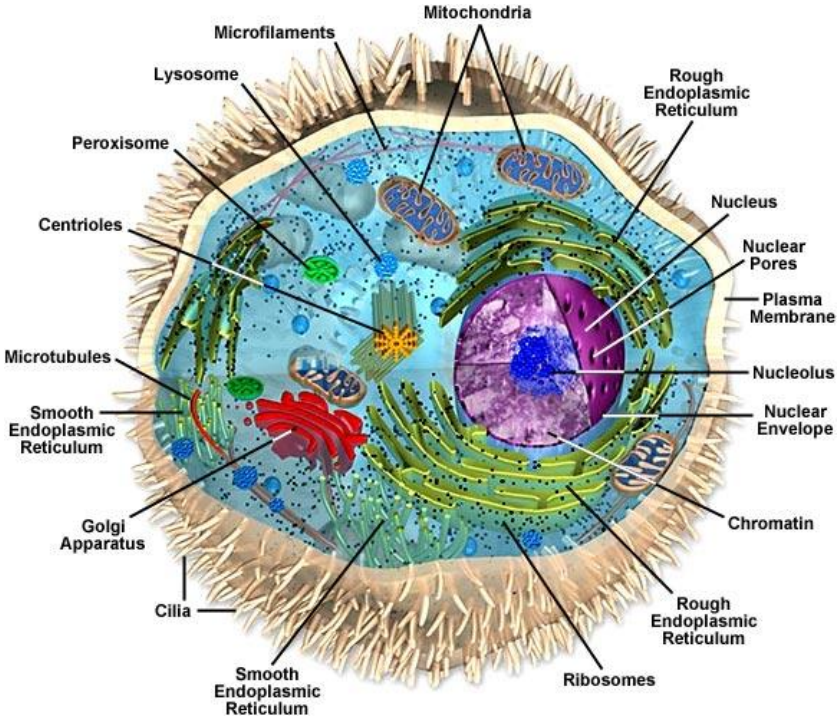

Figure 2.1: This is a typical eukaryotic cell. It ranges in size between 1 and 100 micrometers and is surrounded by a plasma membrane, which forms a selective barrier allowing nutrients to enter and waste products to leave. The cytoplasm contains a number of specialized organelles, each of which is surrounded by a membrane. There is only one nucleus and it contains all the genetic information necessary for cell growth and reproduction. The other organelles occur in multiple copies and carry out the various functions of the cell, allowing it to survive and participate in the functioning of the larger organism [Alberts98].

- **Nucleus** The "controller" of a cell containing genetic information that determines every natural process within an organism.
- **Cell Membrane** Also known as a plasma membrane, this outer layer of a cell assists in the movement of molecules in and out of the cell and plays both a structural and protective role

2.2 DNA structure

The structure, type and functions of a cell are all determined by chromosomes that are found in the nucleus of a cell. These chromosomes are composed of DNA, the acronym for deoxyribonucleic acid.

This DNA determines all the characteristics of an organism, and contains all the genetic material that makes us who we are. This information is passed on from

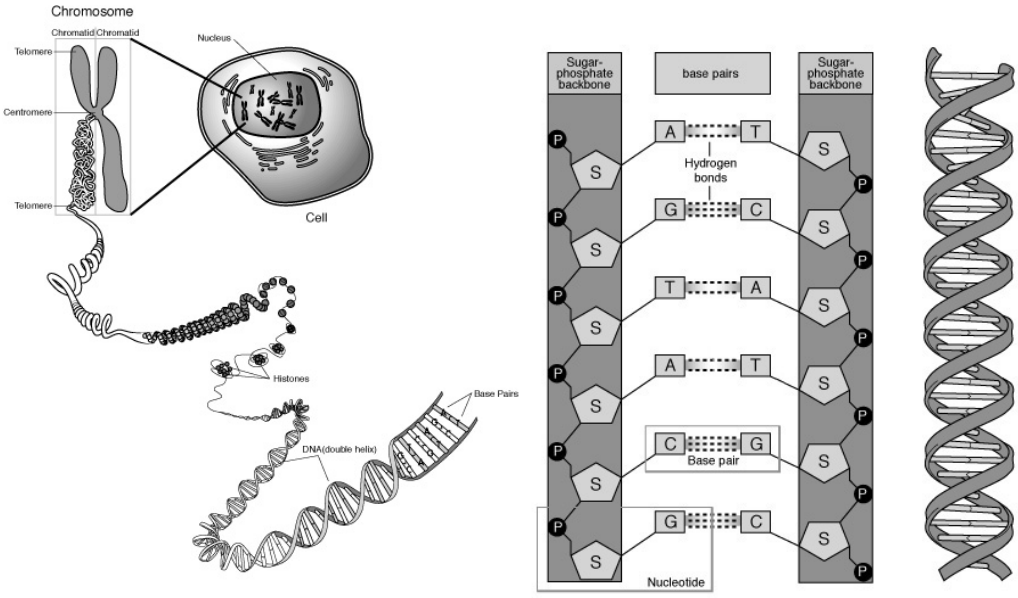

Figure 2.2: Structure of the chromosome of an eukaryotic cell. In the left there is the cell containing the nucleus with chromosomes, which are known to be histone complexed double helices of nucleotides, which are shown in details on the right side [TNHM].

generation to generation in a species so that the information within them can be passed on for the offspring to harness in their lifetime.

DNA is arranged into a double helix structure where spirals of DNA are intertwined with one another continuously bending in on itself but never getting closer or further away (figure 2.2).

There are four different types of nucleotide possible in a DNA sequence: adenine, cytosine, guanine and thymine which can be represented by A, C, G and T. There are billions of these nucleotides in our genome, and with all the possible permutations; this is what makes us unique. Nucleotides are situated in adjacent pairs in the double helix nature mentioned. The following rules apply in regards to what nucleotides pair with one another.

- There are four possible types of nucleotide, adenine, cytosine, guanine and thymine
- Thymine and adenine can make up a base pair
- Guanine and cytosine can make up a base pair
- Therefore, thymine and cytosine would NOT make up a base pair, likewise adenine and guanine.

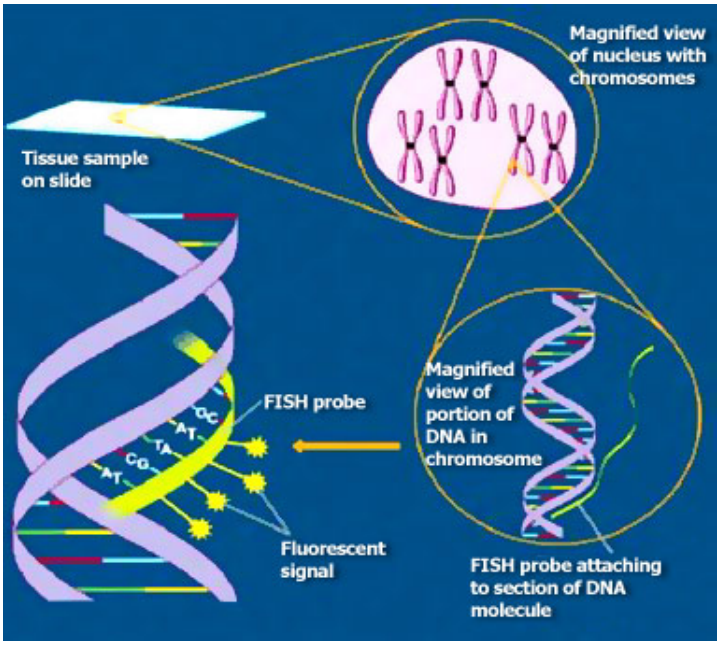

Figure 2.3: Schemmatic of FisH labelling: a DNA sequence of interest is identified among other DNA sequences by pairing it with a complementary sequence used as a "probe", which is labeled with fluorescent dyes [Vysis05].

This continuous sequence, and the sequence they are in, as well as several other factors like methylation determine an organisms' structural, physical and anatomical features [BioOnline].

2.3 Fish Labeling

Hybridization is a process where a DNA sequence of interest is identified among other DNA sequences by pairing it with a complementary sequence used as a "probe". The process depends upon the biophysical properties of DNA nucleotide chains, which will unwind from a double helix at elevated temperatures and will rewind (pair or hybridize) with complementary sequences at lower temperatures.

Fluorescence in situ hybridization (FISH) is a type of hybridization in which a DNA "probe" is labeled with fluorescent molecules so that it can be visualized with a microscope. The word "in situ" means that the hybridization occurs "in place", in this case, within the nucleus of specimen cells that have been fixed to a microscope slide (figure 2.3).

To conduct a FISH analysis, one heats fixed cells mounted on a microscope slide to unwind and denature their chromosomal DNA in order to open the DNA

double strand for probe binding. After adding the probe, the specimen cells are then cooled to allow the DNA probe to hybridize with its complementary target DNA. Once hybridized, the fluorescent molecules on the probe will show precisely where their target DNA lies along a chromosome. Depending upon the design of the probe DNA, one can detect many types of genetic changes [Vysis05].

2.4 HeLa cells

In biological and medical research, a HeLa cell is a cell which is derived from cervical cancer cells taken from an African American woman named Henrietta Lacks. The cervical cancer cells from Ms. Lacks were circulated (without her knowledge or permission) by George Gey. These cancer cells are considered "immortal" (that is, they do not die of old age and can divide an unlimited number of times, unlike most other human cells), and have been grown in cell culture in an unbroken lineage ever since.

This cell line was propagated for use in cancer research. Initially, the cell line was said to be named after a "Helen Lane", in order to preserve Lacks's anonymity. The cells proliferate abnormally rapidly, even compared to other cancers. They are used as model cancer cells and for studying cellular signal transudation. HeLa cells have proven difficult to control. They sometimes contaminate other cell cultures growing in the same laboratory, interfering with biological research.

The degree of contamination is unknown, because few researchers test the identity or purity of already-established cell lines. It has been claimed that a substantial fraction of in vitro cell lines are actually HeLa, their original cells having been overwhelmed by a rapidly growing population derived from HeLa contaminant cells. It has been estimated that the total mass of HeLa cells far exceeds that of the rest of Henrietta Lacks' body. Some researchers have argued that these cells are a separate species, because they reproduce and spread on their own; in 1991 it was named and described as Helacyton gartleri.

On Oct. 4, 1951, Henrietta Lacks died of cervical cancer at Johns Hopkins University Hospital in Baltimore. But Lacks will live forever in laboratories and research centers worldwide that use her unique, immortal cells for medical research. The cells of her cancer, known as HeLa cells, were the first human cells discovered to thrive and multiply outside the body, seemingly forever, allowing researchers to conduct experiments previously impossible [Hopkins00]. However, the karyotype of HeLa cells has been changed during culturing in different laboratorys. So today HeLa cells differ significantly from the original cell and differ between laboraories who have estabished this cell line for routine use in research.

2.5 Mouse embryos

The movement of mouse genetics from a minor field of study to the forefront of modern biomedical research was catalyzed by the recombinant DNA revolution, which began 20 years ago and has been accelerating in pace ever since. With the ability to isolate cloned copies of genes and to compare DNA sequences from different organisms came the realization that mice and humans (as well as all other placental mammals) are even more similar genetically than they were thought to be previously. An astounding finding has been that all human genes have counterparts in the mouse genome which can almost always be recognized by cross-species hybridization. Thus, the cloning of a human gene leads directly to the cloning of a mouse homolog which can be used for genetic, molecular, and biochemical studies that can then be extrapolated back to an understanding of the function of the human gene. In only a subset of cases are mammalian genes conserved within the genomes of Drosophila or C. elegans.

Among mammals, the mouse is ideally suited for genetic analysis. First, it is among the smallest mammals known with adult weights in the range of 25-40 g, 2,000-3,000-fold lighter than the average human adult. Second, it has a short generation time - on the order of 10 weeks from being born to giving birth. Third, females breed prolifically in the lab with an average of 5-10 pups per litter and an immediate postpartum estrus. Fourth, an often forgotten advantage is the fact that fathers do not harm their young, and thus breeding pairs can be maintained together after litters are born. Fifth, for developmental studies, the deposition of a vaginal plug allows an investigator to time all pregnancies without actually witnessing the act of copulation and, once again, without removing males from the breeding cage. Finally, most laboratory-bred strains are relatively docile and easy to handle.

Investigations of the mouse were greatly overshadowed during the first 80 years of the 20th century by studies in other species, most prominently, the fruit fly Drosophila melanogaster. The reasons for this are readily apparent. Individual flies are exceedingly small, they reproduce rapidly with large numbers of offspring, and they are highly amenable to mutagenesis studies. In comparison to the mouse, the fruit fly can be bred more quickly and more cheaply, both by many orders of magnitude. Until the 1970s, Drosophila provided the most tractable system for analysis of the genetic control of development and differentiation. In the 1970s, a competitor to Drosophila appeared in the form of the nematode, Caenorhabditis elegans, which is even more tractable to the genetic analysis of development as well as neurobiology. So why study the mouse at all?

The answer is that a significant portion of biological research is aimed at understanding ourselves as human beings. Although many features of human biology at the cell and molecular levels are shared across the spectrum of life on earth, our more advanced organismal-based characteristics are shared in a more limited

fashion with other species. At one extreme are a small number of human characteristics - mostly concerned with brain function and behavior - that are shared by no other species or only by primates, but at a step below are a whole host of characteristics that are shared in common only with mammals. In this vein, the importance of mice in genetic studies was first recognized in the intertwined biomedical fields of immunology and cancer research, for which a mammalian model was essential. Although it has long been obvious that many other aspects of human biology and development should be amenable to mouse models, until recently, the tools just did not exist to allow for a genetic dissection of these systems [Silver95].

3 Microscopic imaging

3.1 Epifluorescence microscopy

In typical microscopic imaging systems the image is obtained by measuring the light distribution at a large distance from the sample in comparison to the wavelength of light. The light from the sample has passed an optical system and in the image plane the intensity is measured. This technique is often called widefield microscopy in contrast to near field microscopy which tries to determine the light intensity distribution directly in the vicinity of the object under observation. In the case of widefield fluorescence microscopy the process of image formation can be described by an incoherent addition of the individual intensity images of every fluorescent molecule. The reason for this incoherent addition is the loss of phase coherence in the emitted fluorescence light. This has to be seen in contrast to other microscopic methods such as digital interference contrast or phase contrast microscopy which make use of the phase relationships of the light waves in the image plane.

The fact that the images of the fluorescent molecules can simply be added can also be described as a convolution of the fluorescence density distribution in the sample with the point spread function (PSF) of the optical image system. This simple linear process of image formation is one reason for the successful application of image restoration techniques which can calculate details of the specimen structure from the measured intensity distribution. For the reconstruction, knowledge about the process of image formation is used. The image is modeled as a convolution of the specimen structure with the PSF.

The structure of a typical widefield epi-fluorescence PSF is characterized by the detected integral intensity of each plane perpendicular to the optical axis being constant. A de-focused sample will only be blurred, but its overall position will still remain about the same. This makes it impossible to discriminate the position of a plane-like fluorescent object by a standard widefield microscope which illuminates the whole imaged volume simultaneously [Heintzmann99].

3.2 Confocal microscopy

To overcome some of the described disadvantages of standard widefield fluorescence microscopy, confocal microscopy had been invented [Minsky61],

[Cremer78], [Carlsson87]. The idea is to illuminate one diffraction limited spot at a time and to acquire a fluorescence signal only from this region, by forcing the fluorescence light to pass through a confocally aligned small pinhole in front of the detector. A fluorescent molecule has a probability of excitation proportional to the light intensity at its position. The probability of detecting an emitted photon is proportional to the detection efficiency which again, due to the confocal detection pinhole, depends on the position of emission in space. Both of this probabilities can be described by appropriate PSFs. The overall detected signal is thus obtained by a multiplication of those two PSFs (illumination and detection).

$$PSF(x,y,z) = PSF_{illumination}(x,y,z) \times PSF_{detection}(x,y,z)$$

If the different wavelengths of illumination and detection are not taken into account, and the pinhole in front of the detector is sufficiently small, the overall PSF can be approximated by a squared PSF of a normal widefield microscopic system.

$$PSF(x,y,z) = PSF^2_{widefield}(x,y,z)$$

This leads to the optical sectioning quality of a confocal microscope. An object which is out of focus will also be diminished in its integral intensity. The relative integral of a squared blurred signal is much lower than the integral of a blurred intensity because of this multiplication. A plane-like fluorescent object can now easily be discriminated, since the illumination spot will only be small in diameter if the plane is in focus. Only in this case the full fluorescence signal will pass the aligned pinhole in front of the detector. Because of the approximate squaring of the PSF compared to standard microscopy also the lateral extension of the PSF can be reduced and thus the resolution is higher.

One disadvantage of these confocal systems is that it is necessary to have an intense light source which can easily be focused to a small spot. Therefore in most confocal systems lasers are used for illumination. Another drawback is the necessity to scan the illumination spot in three dimensions through the sample. This is achieved either by moving the sample under the microscope (object scanning) or by tilting the angle under which the illumination light illuminates the objective lens system (beam scanning). Often a combination of both methods is used: lateral beam scanning and axial object scanning. Since the maximum useful illumination intensity in fluorescence microscopy is limited by fluorescence saturation, the data acquisition speed of single spot confocal systems is rather restricted. At least some photons per voxel are needed to obtain an image.

Nevertheless, confocal microscopy has become a commonly used tool for three dimensional microscopy with widespread use in biology as well as clinical applications [Heintzmann99].

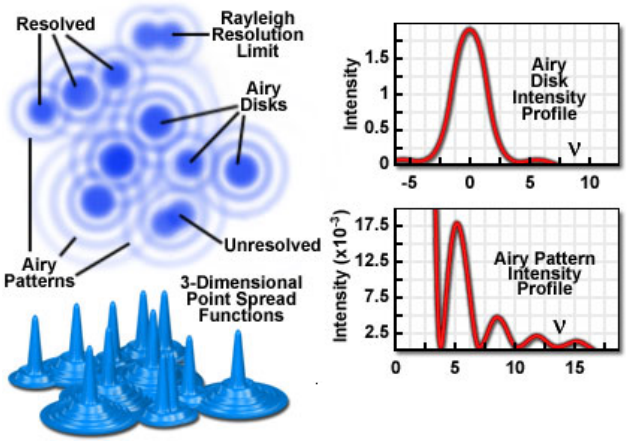

Figure 3.1: Point spread function and airy disk of a microscope used for resolution determination [Olympus].

3.3 Optical resolution

All optical microscopes, including conventional widefield, confocal, and two-photon instruments are limited in the optical resolution that they can achieve by a series of fundamental physical factors. In a perfect optical system, resolution is restricted by the numerical aperture of optical components and by the wavelength of light, both incident (excitation) and detected (emission).

A useful approach to the concept of optical resolution is based on consideration of an image formed by two point-like objects, under the assumption that the image-forming process is incoherent, and that the interaction of the separate object images can be described using intensity point spread functions. The resulting image is then composed of the sum of two Airy disks (figure 3.1). Resolution defines the distance between this two point like spots whose diffraction images could just be separated. For the Rayleigh-criteria this is fulfilled if the principal intensity maximum of one coincides with the first intensity minimum of the other. In lateral direction the distance of the object is then equal to the Airy disc radius.

The resolving power of a lens is ultimately limited by diffraction effects. The lens' aperture is a "hole" that is analogous to a two-dimensional version of the single-slit experiment; light passing through it interferes with itself, creating a ring-shaped diffraction pattern, known as the Airy pattern, that blurs the image. An empirical diffraction limit is given by the Rayleigh criterion:

$$\sin(\theta) = 1.22\,\frac{\lambda}{d}$$

where θ is the angular resolution, λ is the wavelength of light, and d is the diameter of the lens. The factor 1.22 is derived from a calculation of the position of the first dark ring surrounding the central Airy disc of the diffraction pattern.

For a ideal lens of focal length f, the Rayleigh criterion yields a minimum spatial resolution, Δl:

$$\Delta l = 1.22 \, \frac{f\lambda}{d}$$

For a microscope the resolution D depends on the angular aperture α:

$$d = \frac{1.22 \, \lambda}{2n\sin(\alpha)}$$

Here α is the collecting angle of the lens, which depends on the width of objective lens and its distance from the specimen, n is the refractive index of the medium in which the lens operates, λ is the wavelength of light illuminating or emanating from the sample. Introducing the numerical aperture (NA) of the objective which is defined to be $NA = n\sin(\alpha)$ leads us to

$$d = 0.61\frac{\lambda}{NA}.$$

Also common used is the resolution definition as full width at half maximum (FWHM) of the point spread function (PSF). Resolution in the microscope is directly related to the FWHM dimensions of the microscope's point spread function, and it is common to measure this value experimentally in order to avoid the difficulty in attempting to identify intensity maxima in the Airy disk. Measurements of resolution utilizing the FWHM values of the point spread function are somewhat smaller than those calculated employing the Rayleigh criterion. Table 3.1 shows formulas and example values for the resolution of epifluorescence microscopes [Neuhaus98].

Resolution	Rayleigh criteria		FWHM criteria	
Lateral	$0.61\frac{\lambda}{NA}$	231 nm	$0.52\frac{\lambda}{NA}$	197 nm
Axial	$2\frac{\lambda}{NA^2}$	541 nm	$1.77\frac{\lambda}{NA^2}$	479 nm

Table 3.1: Resolution of widefield epifluorescence microscopes: Formulas and theoretical resolution for a microscope with λ = 530 nm and NA = 1.4

3.4 Sampling rate

The fact that all digital microscopy images are acquired, processed, and displayed in the realm of discrete partitions, or pixels, as opposed to being treated as a continuous representation of the specimen data is not a problem of fundamental significance, but rather is a practical matter of imaging technique. As long as the

microscope is operated in accordance with applicable sampling theory, which governs the sampling interval in space or time that is required to reproduce features of interest with sufficient contrast, there is no significant limitation. The sampling criterion most commonly relied upon is based on the well known Nyquist Theorem [Nyquist28], which specifies the sampling interval required to faithfully reconstruct a pure sine wave as a function of its frequency.

In practical operation of the microscope, there is often some uncertainty in estimating the highest frequency that should be of concern in the specimen. Many specimens have sharply defined edges, and numerous features that contribute extremely high-frequency components to the signal. The Airy intensity distribution function or Gaussian distribution imposed by optical elements blurs these components to the extent that detail appears only within the optical resolution limit. Failure to sample all of the frequency components below the limit can produce image errors, although it is unnecessary to sample at the higher frequencies, which will no longer carry specimen information following optical transfer. In some cases, specimens should be sampled at more than 2.3-times the highest information frequency to allow for the possibility that the highest frequency was misjudged. The highest frequency to be sampled (f) is imposed by the optical system and for a particular resolution (r) specification:

$$f = \frac{1}{r}.$$

In order to preserve all of the information transferred by the optical system to the sampling (digitizing) stage of the microscope, the pixel size must be smaller than the inverse of 2.3-times the cut-off frequency ($f_{cut-off}$):

$$PixelSize < \frac{1}{2.3\ f_{cut-off}}$$

An accurate representation of specimen features, within the limits imposed by the experiment, requires use of a spatial sampling frequency and electronic properties, such as bandpass, which are matched to the optical resolution of the system. Usually the optical resolution is primarily determined by the wavelength of the light and the numerical aperture of the objective [Olympus]. Using the FWHM as microscopic resolution (table 3.1) results in a minimal voxel size of 86nm lateral and 208nm axial for a objective with NA = 1.4 and λ = 530nm.

3.5 Fluorescent dyes

Since this work is about resolution improvement in fluorescence microscopy, some basic information about fluorescence is given here. As will be explained, there are major differences between an ideal fluorescence system such as individual

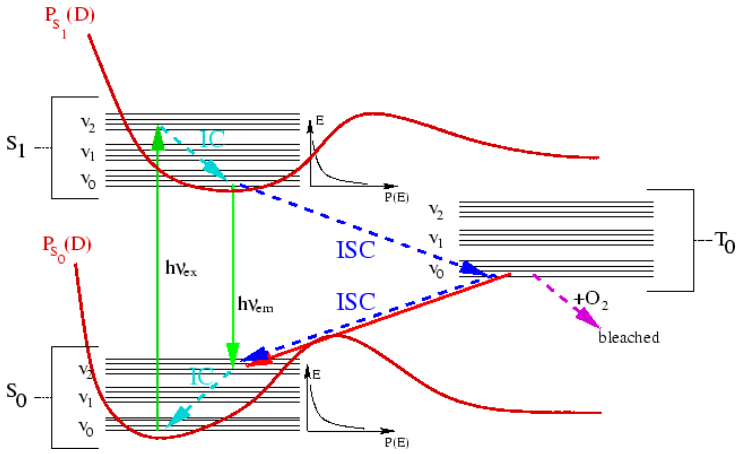

Figure 3.2: Schematic energy level diagram of a fluorescent molecule. S_0 and S_1 are the electronic levels which consist of multiple vibrational levels (marked with v, not drawn to scale). The vibrational levels can further be divided into rotational levels. T_0 marks the first electronic triplet state [Heintzmann99].

molecules in a gas and fluorescence in biology, where fluorophores are usually kept in aqueous solution.

In thermal equilibrium the molecules are distributed in one of the lower levels of the electronic singlet (S_0) level. This equilibrium distribution is depicted to the right of the singlet energy states in a small curve in figure 3.2. The energetic width of this distribution depends on the temperature and can be estimated to equal about $\frac{1}{40}\,eV$ at room temperature. If a molecule is excited by the illuminating light of a matching frequency, it will be transferred to the electronic S_1 level. This transition from S_0 to S_1 can be assumed to be instantaneous. Transitions can also occur to higher electronic states, but they typically show a rapid radiationless decay into the S_1 state.

When the molecule is excited, its electron density distribution changes. This quick change has not yet affected the positions of the atomic nuclei. The potential energy of the whole system (electrons and nuclei) shows a dependence on the positions of the nuclei. Such potential curves are depicted for the two singlet states in figure 3.2 by the dark red curves labeled $P_{S_{0,1}}(D)$. The distance D of two (for simplicity) atomic nuclei is drawn horizontally in these curves and the potential energy of the combined system is shown on the vertical axis. When the excited electronic level is reached, the lowest possible excited state energy is at a different inter atomic nuclei distance D. Because the electronic transition is very fast (a few fs) the nuclei have no time to readjust their position, and the most probable electronic transition will be into an excited vibrational state of the total system. This is called the “Franck-Condon-Principle”. The probability of this transition

depends on the overlap integral of the associated eigenstates and the state density near the final energy of this transition. This principle is an analogue to "Fermi's Golden Rule" in solid state physics. Described in a more classical way, the nuclei "feel" electric forces after the instantaneous electronic redistribution and thus are at first vibrating.

Molecules in the S_1 level have the possibility of emitting a fluorescence photon by a transition to the electronic ground state. The typical transition time for this process is called fluorescence lifetime and is usually in the nanosecond range. The vibrational de-excitation of the molecule can therefore be assumed as having already occurred.

The "Franck-Condon-Principle" is again applicable for the emitting transition into the ground state. The overlap integral of the new equilibrium state to a vibrational not excited S_0 state is very small. The final state in S_0 will most probably be a vibrational excited state. Taking excitation and de-excitation together, the energy of the emitted light ($h\nu_{em}$) is most likely much lower than the typical excitation energy $h\nu_{ex}$.

The probability for fluorescence emission of an excited fluorophore is called its quantum efficiency (QE). In addition to the light emitting fluorescence decay, there are other ways of decay for the electronic excited state. It can undergo a radiationless transition into the electronic ground state (not shown in figure 3.2) or it can perform a transition into one of the electronic triplet states by inter-system crossing (ISC). ISC is shown in figure 3.2 as a dashed arrow into and out of T_0. The radiative transition from the triplet into the ground state (red arrow) has a small transition rate because such a spin-flip is quasi-forbidden. This is called phosphorescence.

In fluorescence spectra of molecules in a gas, the individual vibrational bands can be observed even at room temperature. In solution, however, none of these distinct line spectra can be detected. The vibrational and rotational energy levels are not visible. Due to the temperature dependent occupation of energy states (small graph to the right of the electronic levels in figure 3.2) rotational levels are smeared out even in a gas at room temperature. In solutions there is, however, a much larger effect of smearing. If total spectra of many fluorescent molecules are measured, each of these molecules has a specific momentary surrounding. These specific surroundings (the relative positions of the solvent molecules) can substantially shift the positions of the individual excited electronic states. The total fluorescence of the sample in solution can thus be completely smeared out so that no individual vibrational or rotational levels are distinguishable. Even if only a small number of molecules is observed, the individual levels cannot be observed at room temperature, because the surroundings change very rapidly in time [Heintzmann99].

3.6 Tomography

The concept of Tomography was first published as early as 1826, by Abel, a Norwegian mathematician, for an object with axi-symmetrical geometry [Abel26]. In 1917, an Austrian mathematician, Radon, extended Abel's idea for objects with arbitrary shapes [Radon17].

A number of applications of tomographic imaging of process equipment were described in the 1970's, but generally these involved using Ionising Radiation from X-ray or isotope sources, and were not satisfactory for the majority of process applications on a routine basis because of the high cost involved and safety constraints. Most of the radiation-based methods used long exposure times which meant that dynamic measurements of the real time behaviour of systems were not feasible.

Computed Tomography (CT)

CT imaging (also called CAT scanning for Computed Axial Tomography) was invented in 1972 by Godfrey Hounsfield in England. Hounsfield used gamma rays (and later x-rays) and a detector mounted on a special rotating frame together with a digital computer to create detailed cross sectional images of objects [Hounsfield73]. Hounsfield's original CT scan took hours to acquire a single slice of image data and more than 24 hours to reconstruct this data into a single image. Today's state-of-the-art CT systems can acquire a single image in less than a second and reconstruct the image instantly.

Electron Microscope Tomography

Electron tomography refers to the reconstruction of the 3D structure of specimens using transmission electron micrographs [Frank92].

The goal of electron tomography is to generate a three dimensional model of an object from a series of tilt projections. To have adequate data for reconstruction requires a large number of projections (> 60) to be collected over a wide tilt range ($\pm 70^\circ$). Unfortunately most low-Cs TEM polepieces do not allow such a large range of tilt with a standard holder, this typically limits tilt to $\pm 40^\circ$.

Limited tilt results in the degradation of resolution, especially in the Z (depth) direction, and introduction of reconstruction 'artifacts'. Therefore modification to the backprojection routines, or post-processing of the three dimensional dataset is required to achieve adequate results. The ideal solution to such resolution problems is the use of a high-tilt tomography stage.

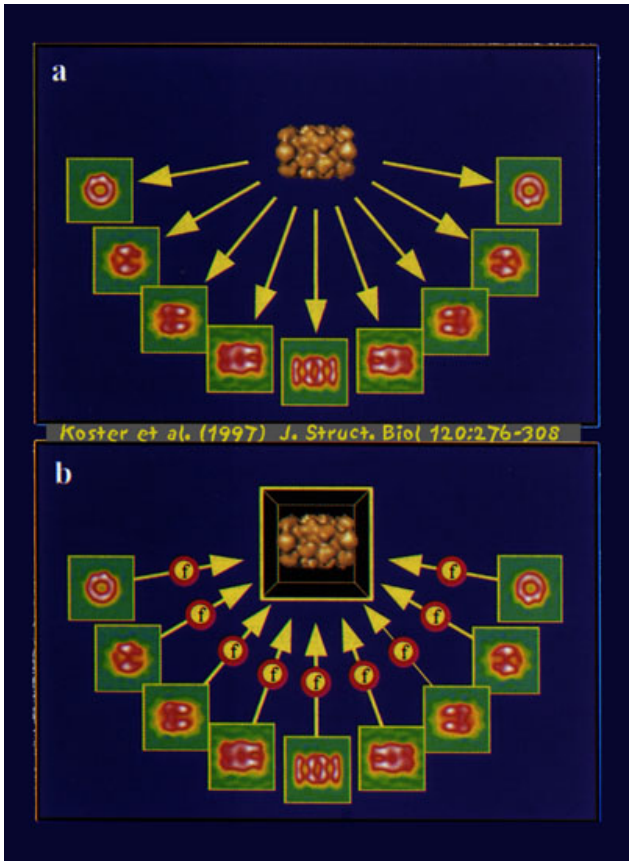

Figure 3.3: The principle of electron tomography is not that different from CAT scan medical imaging: 2D-projections of the 3D object, tilted up to 70 degrees in the electron microscope, are recorded and after alignment are electronically reassembled using the so-called weighted back-projection algorithm.

Optical Tomography

In general, a shortcoming of 3D-imaging by far-field light microscopy is the spatial anisotropy of resolution that can be found for nearly all kinds of instruments. In most commercially available systems the resolution along the optical axis (axial resolution) is worse than the resolution in the focal plane (lateral resolution). As a reasonable approach to overcome shortcomings of the resolution of anisotropy tilted view microscopy has been suggested. The first system that allowed tilting of the specimen in a microscope was constructed by [Skaer75], who rotated the whole microscope slide with the objects of interest. Therefore, the tilting range yielding good optical quality was relatively low (up to $\pm$ 15°). In another device

the slide was omitted completely and the objects (mostly cells or cell nuclei) were placed into a glass capillary that could be rotated up to 360° [Bradl92] [Bradl94]. However, the application of the capillary revealed some disadvantages. The sample had to be prepared in suspension and sucked into the capillary. This constraint could not be easily adapted to any labeling technique, as for instance to fluorescence in situ hybridization (FISH) of specific chromosome regions. Moreover, the suspension had to fulfill additional optical conditions. Because the capillary brought another curved glass surface into the light path, appropriate immersion fluids inside and outside the capillary were necessary to carefully match the refraction index of the glass. Unfortunately, the conditions of specimen preparation and immersion fluids were most often contradictory. Therefore, the capillary has been replaced by a glass fiber on which the objects can be fixed [Bradl96a][Bradl96b] so that a standard coverglass can be placed between the objective lens and the observed objects to obtain better imaging properties. A large tilting range (up to approximately $\pm$ 60°) can be preserved also for high numerical aperture (NA) oil immersion objectives that have a very short working distance of typically 190 μm [Kozubek02]. Within this tilting range angular series of images, in which the same object structures are viewed with the poor axial and the best lateral resolution, can be acquired.

4 Image analysis

4.1 Evaluation of distances

Frequently the objects under observation (such as genes inside the cell nucleus) do not have a predefined orientation to the optical axis of the microscope. If the position of two objects are compared, the only interesting parameter which can be extracted from the evaluation is the distance between them. An interesting question is therefore to estimate the error of a known mean distance from two localized objects with known localization precisions for the in-plane lateral (XY) and axial (Z) directions. The calculation of the error assuming randomly in space distributed orientations is described in [Bradl96a]. In the following a more accurate calculation on this matter will be presented:

The 3D-distance d is defined in terms of the coordinates of point p and point q as

$$d = \sqrt{(x_p - x_q)^2 + (y_p - y_q)^2 + (z_p - z_q)^2}$$

The associated error Δd is calculated as a function of the individual errors $\Delta x_p \ldots \Delta z_q$ by using the Gaussian propagation of errors. Here the implicit assumption is made that the distance d is large compared to the individual localization errors. If the distance between the spots is comparable to the localization errors, the situation is more complicated. For a treatment of the general case see [Manders94].

When it is assumed that the localization precisions of points p and q along all in-plane coordinates are identical $\Delta x_p = \Delta y_p = \Delta x_q = \Delta y_q = \Delta x$ and the axial localization precision also corresponds $\Delta z_p = \Delta z_q = \Delta z$, the error can be written as:

$$\Delta d = \sqrt{2\left(\frac{\partial d}{\partial x_p}\right)^2 \Delta x_p^2 + 2\left(\frac{\partial d}{\partial y_p}\right)^2 \Delta y_p^2 + 2\left(\frac{\partial d}{\partial z_p}\right)^2 \Delta z_p^2}$$

Calculation yields:

$$\Delta d = \frac{\sqrt{2\left(x_p - x_q\right)^2 \Delta x^2 + 2\left(y_p - y_q\right)^2 \Delta x^2 + 2\left(z_p - z_q\right)^2 \Delta z^2}}{d}$$

Introducing the radial distance $r = \sqrt{x^2 + y^2}$ measured in the plane obtained by a

projection along the optical axis, the error becomes

$$\Delta d = \frac{\sqrt{2r^2\Delta x^2 + 2z^2\Delta z^2}}{d}$$

z denotes the axial difference of the two spots. Δx and Δz still denote the precision of individual localizations of spot p or q. For a certain angle Θ of orientation to the optical axis of the line connecting the two spots, it can be written as

$$\Delta d(\Theta) = \frac{\sqrt{2d^2\sin(\Theta)^2\Delta x^2 + 2d^2\cos(\Theta)^2\Delta z^2}}{d}$$

$$= \sqrt{2\sin(\Theta)^2\Delta x^2 + 2\cos(\Theta)^2\Delta z^2}$$

This has to be integrated with equal weights on the sphere of possible orientations:

$$\Delta d_{Mean} = \frac{\int \Delta d(\Theta) 2\pi \sin(\Theta) d\Theta}{4\pi} \tag{4.1}$$

The integral can be solved analytically using Maple, but its result is rather complicated. It can however quite accurately be approximated by the simple mean value of the lateral ($\Delta x_d = \sqrt{2}\Delta x$) and axial ($\Delta z_d = \sqrt{2}\Delta z$) error of the distance vector d:

$$\Delta d_{Mean} \cong \frac{\Delta x_d + \Delta z_d}{2} \tag{4.2}$$

The error in this approximation is below 10% for $\Delta z_d > \Delta x_d$.

4.2 Likelihood maximization

To obtain the highest possible resolution in microscopic imaging, the measured datasets can be improved by using various deconvolution methods [Schaefer97]. Since the optical transfer function (OTF) equals zero above a limiting absolute spatial frequency, deconvolution methods which are based on a division in Fourier-space are not very successful and tend to amplify the noise.

The maximum likelihood (ML) method for image reconstruction is a widely used tool from mathematical statistics which can be adapted to the needs of different imaging modes. It can be based on the assumption of an underlying Poisson-distributed process of image (or signal) formation. Because the inversion of the equations of image formation including the photon statistics is hard or very time consuming, an iterative process is frequently used to obtain an approximation to the solution.

There is a drawback in the maximum likelihood deconvolution which can be attributed to the *ill-posedness of the problem* [Holmes95]. The standard ML-procedure is known to not converge towards the correct sample structure in the

presence of photon noise. The reason is that the ML-algorithm looks for the best guess of any structure (including impossible ones) which can produce the best likelihood for the measured intensities. To obtain useful results it is therefore preferable to place constraints on the sample structure. A fluorescence distribution is known to be greater than or equal to zero at all points in space. It is useful to constrain the reconstructed sample to positive values. Other constraints can further enhance the image quality as for example the method of sieve kernels [Markham97].

In microscopic imaging the ML-deconvolution method is being used and studied since some time [Richardson72]. The techniques have been further improved to allow reconstruction without a previous knowledge of the point spread function (PSF) by simultaneously reconstructing the sample and PSF from the measured image data (blind deconvolution [Holmes95], [Holmes94]).

The maximum likelihood method used for reconstruction of the three dimensional data as well as for the determination of target positions are extensions to normal maximum likelihood algorithms described elsewhere [Kempen97]. The goal of any maximum likelihood based algorithm is to find a solution for its unknown parameters which maximizes the probability of the measured values being obtained if these parameter values are true (this is called the likelihood). This computable likelihood depends on the model chosen and especially on the part of the model which describes the statistics associated with the measured events.

4.3 General ML formula

The parameters can in principle be chosen freely in the model. In the case of image reconstruction, the model usually consists of a grid of intensity values and the measured values are connected with predicted observation intensities of the model via photon statistics. The statistics is Poisson distributed with probability P_i to measure the i^{th} value M_i if its expectation value is E_i:

$$P_i = \frac{E_i^{M_i}}{M_i!} e^{-E_i}$$

The n unknown parameters in the model are called p_k. E_i are the predicted observation values and M_i are the measured data values. We can then write the probability to measure these values assuming Poisson statistics as the product of the individual probabilities for any model:

$$P(p_1,\ldots,p_n) = \prod_i \frac{E_i(p_1,\ldots,p_n)^{M_i}}{M_i!} e^{-E_i(p_1,\ldots,p_n)} \tag{4.3}$$

The parameters p_k have to be calculated to maximize $P(p_1,\ldots,p_n)$. Assuming $P(p_1,\ldots,p_n)$ to be continuous and $p_1,\ldots,p_n$ unbounded, the derivation of for-

mula 4.3 with respect to each p_k has to be zero for all k:

$$\frac{\partial P(p_1,\ldots,p_n)}{\partial p_k} = 0$$

Since the logarithm is a monotonous function it will also be maximum, if P_k is maximum:

$$\begin{aligned} 0 &= \frac{\partial ln P(p_1,\ldots,p_n)}{\partial p_k} \\ &= \sum_i \frac{\partial ln\left[\frac{E_i(p_1,\ldots,p_n)^{M_i}}{M_i!}e^{-E_i(p_1,\ldots,p_n)}\right]}{\partial p_k} \\ &= \sum_i M_i \frac{\partial ln E_i(p_1,\ldots,p_n)}{\partial p_k} - \sum_i \frac{\partial E_i(p_1,\ldots,p_n)}{\partial p_k} \\ &= \sum_i \left(\frac{M_i}{E_i(p_1,\ldots,p_n)} - 1\right)\frac{\partial E_i(p_1,\ldots,p_n)}{\partial p_k} \end{aligned} \tag{4.4}$$

Except for the Poisson distribution of the noise, the model itself is not yet specified. If equation 4.4 can be solved for all k, the unknown parameters p_k are determined. The two different maximum likelihood procedures for image restoration and precise measurement of the position will be deduced below from this formula.

The model of generation of expectation values $E_i(p_1,\ldots,p_n)$ is described by the convolution of a virtual high-resolution dataset with the point spread function. The voxel-intensities in the high resolution data cube to reconstruct are taken as the unknown parameters p_k, k numbering the individual voxel. In the case of image reconstruction from microscopic images, the predicted values $E_i(p_1,\ldots,p_n)$ can be calculated through a model, where each predicted value depends linearly of some of the model intensities p_k with a weight factor w_{ik}:

$$E_i(p_1,\ldots,p_n) = \sum_k w_{ik}\, p_k$$

This is simply an overall notation which enables rotating and shifting the model data cube into the appropriate position and convoluting it with the point spread function (PSF) of the microscope.

Substitution of this into formula 4.4 yields for every l the equation:

$$0 = f_l = \sum_i \left(\frac{M_i}{\sum_k w_{ik}\, p_k} - 1\right) w_{il} \tag{4.5}$$

4.4 Richardson-Lucy iteration formula

The determination of the voxel intensities in the high resolution dataset (p_k) from formula 4.5 is very difficult to obtain by direct solution of this large nonlinear system of equations. There is however the possibility to come very close to the true solution by an iterative approach. Formula 4.5 states the final fix-point which the algorithm should try to find. There are now different possibilities to reach this fix-point. The easiest and widely used method is the Richardson-Lucy iteration [Richardson72].

In this method the error of the iteration for a guessed dataset is calculated by applying the right hand side of formula 4.5 to this guess. The result is then multiplied with the associated model parameter p_l and added to it.

$$p_l^{n+1} = p_l^n + f_l^n \, p_l^n$$

As it can easily be seen, there is no further correction, if f_l^n is 0. When the fix-point is reached, the iteration will have converged. To increase the speed of convergence of this algorithm it is very useful to multiply the correction $f_l^n \, p_l^n$ with a global overrelaxation factor q [Lewitt86]. This has however the drawback that the iteration is not any longer guaranteed to be stable, so the overrelaxation factors have to be selected carefully.

This iteration formula can now be interpreted as follows:

- First a nonzero guess data cube is obtained (in algorithm used it is equal to one everywhere).
- Then the E_i are calculated from this guess. This is called the *forward projection*. It consists of rotating and shifting the data cube into the position of observation and convoluting it with the microscopic point spread function $PSF\,(\overrightarrow{x})$. This has to be done for every measured dataset orientation and position. This step computes the values of $E_i\,(p_1, \ldots, p_n)$
- The value of $\frac{M_i}{E_i(p_1,\ldots,p_n)} - 1$ is calculated.
- This correction value is now projected back using the *transposed* indices of w_{ik} (note that in 4.5 the summation is now over the first index i in w_{il}). That means, it is convolved again, but with the space-inverted point spread function $PSF\,(-\overrightarrow{x})$, then rotated and translated backwards into its position in the reconstruction data cube yielding the correction value f_l. It is interesting to note that there are two convolution steps with the point spread function (one normal and one room-inverted) but there is no linear deconvolution step (like Wiener-filtering) in this iterative process.
- The now back projected correction is then applied using $p_l = p_l + q \, f_l \, p_l$.

This method is closely related to other iterative deconvolution approaches as the gradient descent method or the Jansson-van Cittert method [Jähne99, Vol. 3, chapter 39.3]. These methods do, however, try to obtain least square solutions. That means, they assume a Gaussian distributed noise [Heintzmann99].

5 Micro axial tomography

Cell Biology is three dimensional. For this reason more and more research is focused on three dimensional imaging and analysis of the specimen under observation. Confocal fluorescence microscopy allows three dimensional imaging of biological specimen (optical sectioning). But even a confocal microscope still has a limited axial resolution. This anisotropic resolution along the optical axis (z-direction) is a factor of about three worse than the transversal resolution. In many cases this sub-optimal axial resolution is also the weakest chain in data evaluation.

A high and isotropic resolution is desirable for precise imaging and analysis of specimens. To circumvent the fundamental problem of low axial resolution, the technique of optical tomography has been introduced [Shaw89]. By a rotation of the specimen under the microscope, it is possible to acquire a number of different datasets (views), where the axis of reduced resolution points into different directions relative to the specimen. In this way, additional information about the specimen can be measured.

5.1 Tomograph hardware

The currently used tomograph (figure 5.1) [Eipel05] is designed for high precision rotation of glass fibers without lateral movement. The whole device is cut out of one piece of brass, which gives it a high mechanical stability. Newly designed V-shaped grooves, which are vertically adjustable with two screws each, in combination with the horizontal adjustable motor, guarantee the precise alignment of the fiber axis. The device is equipped with a stepper motor for computer controlled rotation of the glass fiber with a digital controller connected to the parallel port. The motor has a tilting angle of 18° per step so that 20 steps correspond to a 360° rotation. The whole apparatus has the footprint of a standard object slide (76 x 22 mm) to be usable with every microscope without additional hardware or difficult adjustments. Of course the tomograph has to be adjusted once after manufacturing to guarantee the precise alignment of the fiber bearings and the motor axis and to avoid lateral movement of the glass fiber during the tilting process. This adjustment has to be changed only if the used specimen are changed to ones with are very different in size, e.g. mouse oocytes and HeLa cells.

The fiber with attached specimen is fixed in the tomograph with the two fiber bearings and a small drop of thermal glue, attached to the motor axis, which is

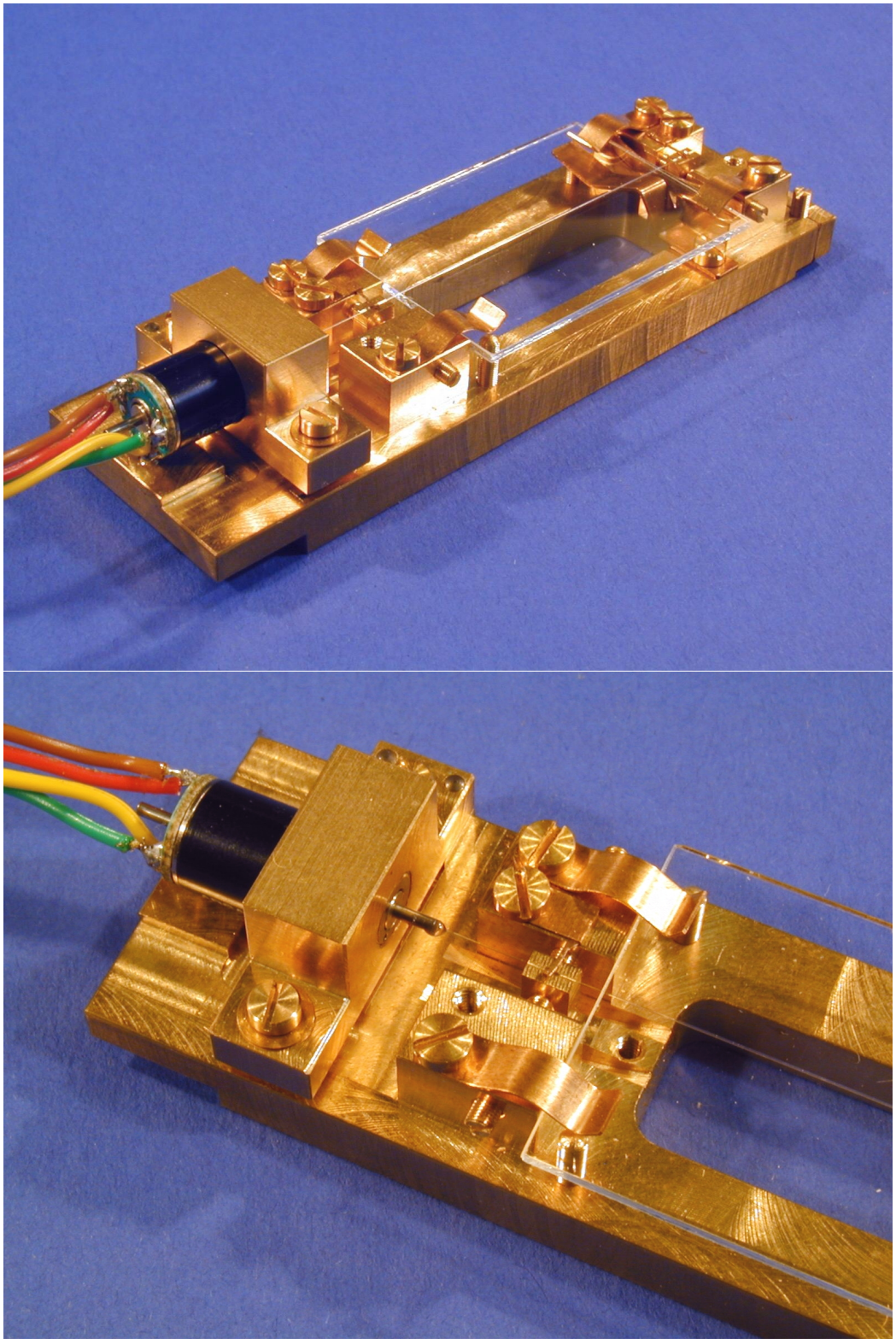

Figure 5.1: Picture of the currently used micro axial tomograph which was manufactured at the mechanical workshop of the KIP. In the left part there is the stepper motor with the horizontal adjustment screw and one of the fiber bearings with vertical adjustment screws, in the right part are the cover glasses and the second fiber bearing.

Footprint (x,y):	76 x 22 mm
Total height:	18 mm
Height between objective and stage:	12 mm
Minimum rotation angle:	18°
Steps for 360° rotation:	20
Fiber diameter:	120 μm
Fiber length:	6000 mm
Visible fiber length:	2000 mm
Visible fiber surface:	754 mm^2
Immersion:	Water, Glycerol, Oil
Embedding medium:	Water, PBS, Glycerol, Vectashield

Table 5.1: Technical data of the tomograph system

slightly warmed with a low temperature soldering iron. It connects the motor axis with the end of the glass fiber. The fiber end is centered on the motor axis by slowly rotating the stepper motor while the thermal glue is cooling down.

5.2 Microscope setup

For this thesis the tomograph was used in combination with two Zeiss wide field microscopes at Heidelberg and Bar Harbor. The software of these microscopes was adapted and the tomograph control was added. This chapter provides an overview of the different used setups.

Heidelberg

The Heidelberg Setup (figure 5.2) is based on a Zeiss Standard 25 microscope which is equipped with a fluorescence unit and a cooled Kappa camera (CF 8 RCC). The fluorescence unit provides different filter sets for DAPI, FITC and TRITC (table 5.2) which have to be changed manually by the user.

Furthermore an motorized Märzhäuser xy stage is mounted on the microscope, which is controlled as well as the motorized z drive with a MC2000 control unit. Images were acquired with a 63x 1.4 oil and a 40x 0.75 air objective. All of the described hardware controllers are as well as the camera connected to a PC which is equipped with a 700 MHz Duron processor and 512 MB of ram.

The software for this microscope is based on the fish2 software developed specially for the acquisition and analysis of FisH stained cells [Kozubek99] [Kozubek01] to which a tomograph control module to acquire images of the specimen on the whole glass fiber was added [Kozubek02]. Additional software was developed for determination of the precise rotation angle between two image stacks

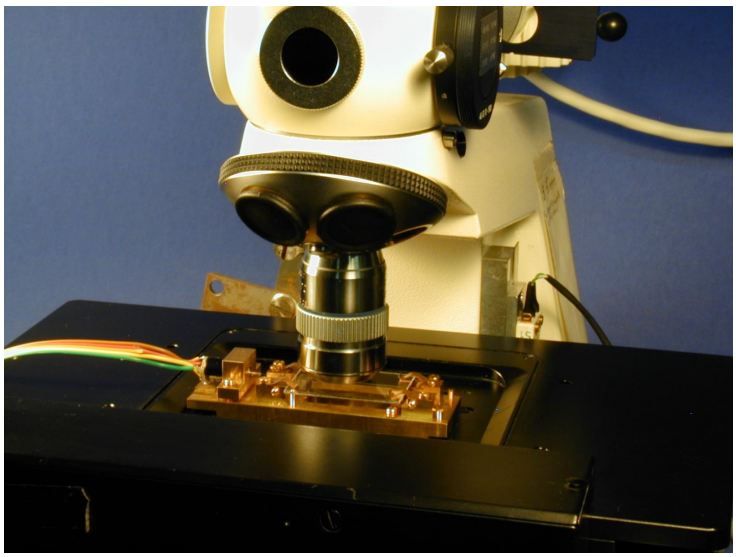

Figure 5.2: The micro axial tomograph in use with a automated Zeiss Standard 25 microscope equipped with fluorescence unit and motorized Märzhäuser stage.

and assignment of the objects after rotation [Matula03].

Dye	$\lambda_{absorption}$ [nm]	$\lambda_{emission}$ [nm]
DAPI	355-375	≥ 397
FITC	450-490	≥ 515
TRITC	530-560	≥ 585

Table 5.2: Wavelengths of the different fluorescence filters at the Heidelberg Zeiss microscope

Bar Harbor

The Bar Harbor hardware is based on a motorized Zeiss Axioplan 2 imaging microscope equipped with a Märzhäuser xy stage and a Zeiss Axiocam MR camera. The microscope provides a motorized filter wheel as well as a motorized objective revolver. Filters are available for DAPI, FITC, TRITC and CY5, the used objectives where 100x 1.4 oil and 63x 1.4 oil. The setup is completed by a PC which is used for controlling the microscope, image acquisition and data analysis.

With this microscope the Zeiss Axiovision 4 software which is able to control the microscope stage, filter wheel and objective revolver as well as the camera for automated image stack acquisition was used. A Visual Basic module to control

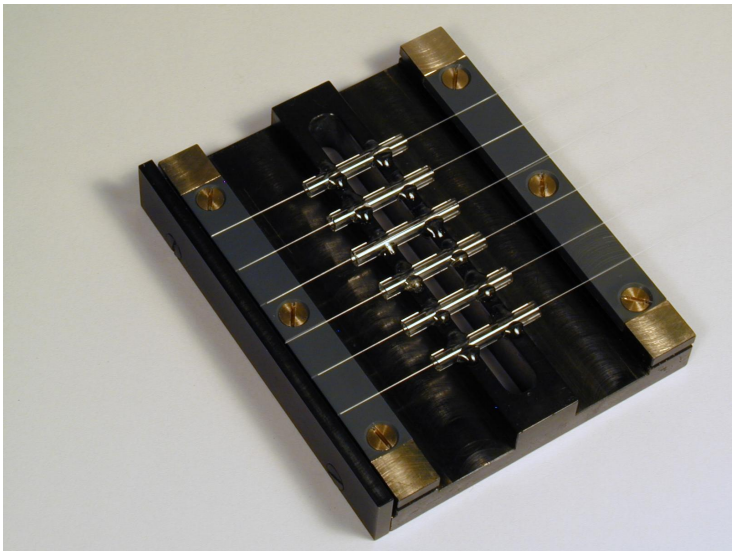

Figure 5.3: Device for attaching specimen to the glass fiber: small glass capillaries in the middle for the specimen suspension and grooves on the left and right to hold the fiber precisely in the center of the capillary.

the tomograph functions was added as part of this thesis, using the macro plugin module of Axiovision (Appendix D).

5.3 Glass fiber preparation

The used glass fibers with a diameter of 125μm are produced very preciseley by the glass-blower of the physics institute. About 50% of the fibers are within an acceptable diameter range of 115μm to 135μm to fit precisely with the tomograph bearings.

The fibres are stored in 50% H_2O + 25% Isopropanol + 25% Ammonia(50%) to keep them very clean (especially lipids could easily cover to whole fiber surface). Also it was found that several cleaning steps with filtered water, ethanol and isopropanol improves the results significant [Staier02].

5.4 Biological specimen preparation

Specimen have to be attached to the fiber strongly enough to stay in place during the tilting movement but not too strongly, because then especially larger cells will become flat. Therefore a special surface preparation has been developed [Staier02]. It consists of a three step procedure (figure 5.4): the reaction starts with

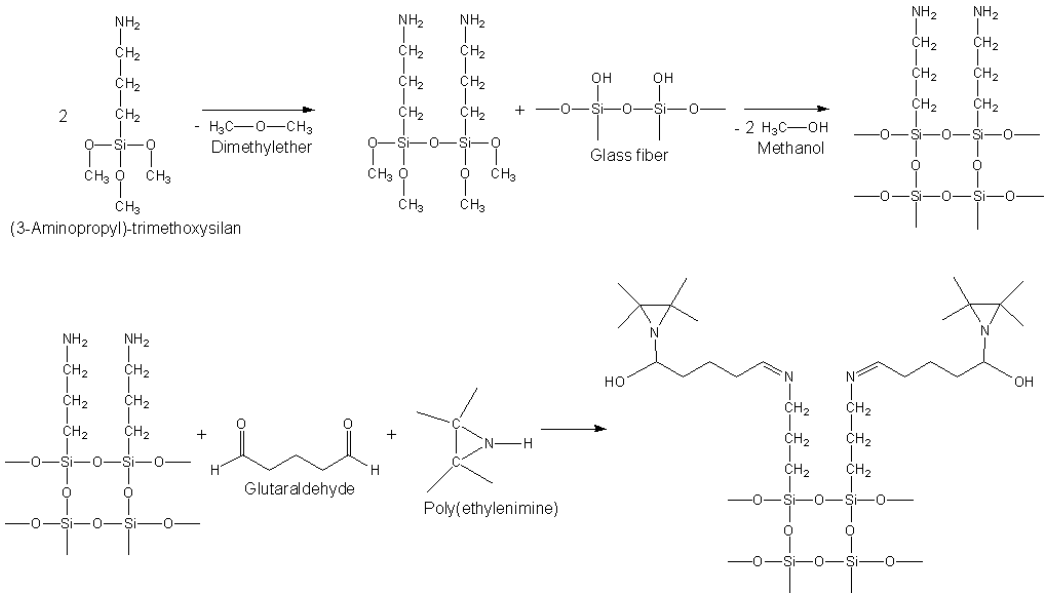

Figure 5.4: Principle of the fiber surface chemistry: the fiber is coated with Aminopropylsilane and Polyethylenimmine, glutraic dialdehyde functions as a cross linker, connecting them with Schiff bases.

condensation of two (3-Aminopropyl)trimethoxysilan with formation of Dimetylether. In the next step the product is linked to the glass fiber by another condensation reaction with formation of methanol. Poly(ethylenimine) is attached to the amino group by glutaraldehyde as cross linker, connecting with Schiff bases. The whole surface preparation protocol can be found in appendix A.

After the fiber surface preparation the specimen (beads or fixed cells) could be attached to it with another special designed device (figure 5.3). It is equipped with small glass capillaries in the middle for the specimen suspension and grooves on the left and right to hold the fiber precise in the center of the capillaries. After the fiber is centered in one capillary about $50\mu l$ of cell suspension is pipeted into it. The cells are then "trapped" by the fiber while moving close to it with brownian motion.

Because special DNA probes are quite expensive, a second device was build to minimize the volume of the needed probes for FisH staining (figure 5.5). It has the same functionality as the fiber preparation capillaries described before: the glass fiber is held precisely in the middle of a special chamber, which can be filled with a fluid. But the fluid chamber of this device has a volume of about $10\mu l$, which is the standard amount of DNA probes used to stain an object slide. Another advantage is the object slide base of this fiber holder: the FisH protocol (appendix B) can be done with an object slide and all equipment which is already available to stain object slides. No further equipment is needed.

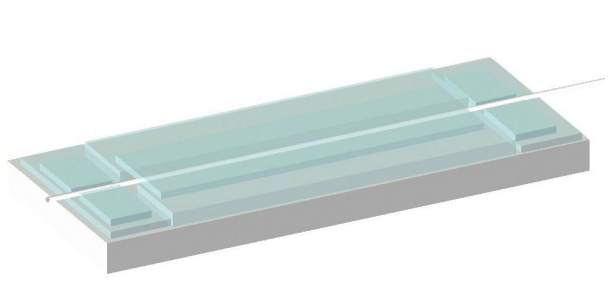

Figure 5.5: Device for the hybridization of specimen attached to the glass fiber with a small DNA probes chamber in the middle and fiber bearings on the left and right.

5.5 Tomograph preparation

The tomograph preparation depends on the size and embedding medium of the objects used. The glass part of the tomograph which is shown in figure 5.6 is easily changeable to be adjusted to different kinds of specimen. It consists of three layers of glass slides: the top layer is a cover glass to separate the specimen from the immersion liquid of the objective which is typically water, glycerol or immersion oil depending on the used objective. The second layer consists of two glass slides which function as spacers and form a channel for the glass fiber in the middle. The third and final layer consists of an object slide as a stable and adjustable subsoil for all the slides above. It can be adjusted by 2 screws on one side, and is held by a spring on the other side of the tomograph.

The thickness of the spacers in layer two has to be chosen depending on the size of the observed specimen to give them enough room above and below the glass fiber and to avoid contacts with the specimen and the glasses above and below the fiber. Experiments showed that for small beads ($< 500nm$) one cover slide with a thickness of typically $170\mu m$ provides enough room ($25\mu m$ above and below the fiber which has a diameter of $120\mu m$). For small biological specimen like HeLa cells, which have a diameter of about $10\mu m$ two coverglasses ($340\mu m$) where used to have more space around the fiber which makes the adjustment of the fiber easier. For large biological specimen like mouse oocytes object slides with a thickness of $1000\mu m$ where used as spacers. Table 5.3 shows all used specimen and used spacers.

The embedding medium in the fiber chamber depends on the specimen used. For beads and fixed HeLa cells 50% Glycerol in H_2O, which has the advantage of not evaporating, was used. For mouse oocytes it was necessary to adapt the tomograph to work with phosphate buffered saline (PBS) as embedding medium which evaporates very fast at the fiber ends and the spaces between the different

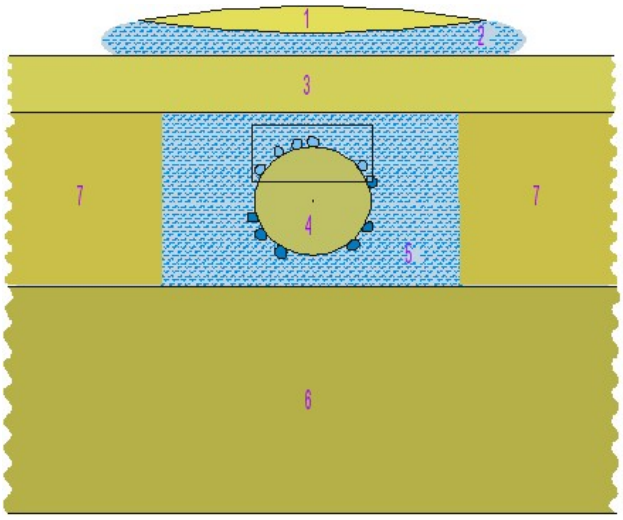

Figure 5.6: Geometry of the fiber within the tomograph. The light passes through a high NA objective lens (1), immersion oil layer (2) and coverglass (3) to the cells fixed onto the fiber (4). The fiber chamber, which is formed by two cover glasses or slides as spacers (7) and and a slide (6), is surrounded with a suitable embedding medium (5). [Kozubek02]

Specimen	Diameter	Tomgraph spacers	Sp. thickness	Rot. angle
Beads	0.2 μm	one cover slide	170 μm	$\pm$ 180°
HeLa cells	10 μm	two cover slides	340 μm	$\pm$ 180°
Mouse oocytes	80 μm	one object slide	1000 μm	$\pm$ 72°

Table 5.3: Technical specifications of the tomograph system depending on the object size

glass layers. To avoid this evaporation the glass slides have to be coated with silane in order to make them hydrophobic, which prevents the water based PBS wicking to the outside. Experiments showed that SurfaSil, using the wipe off protocol, provides the strongest hydrophobic effect.

5.6 Maximal rotation angle

When choosing spacers and adjusting the tomograph the limited working distance of high NA objectives, for example 190μm for a 63x 1.4 oil objective, has to be kept in mind. To acquire the whole specimen this working distance (d_{wk}) has to be bigger or equal than the sum of the spaces above the cover glass for immersion (d_{s1}), between the coverglass and the specimen (d_{s2}), the specimen thickness (d_{sp})

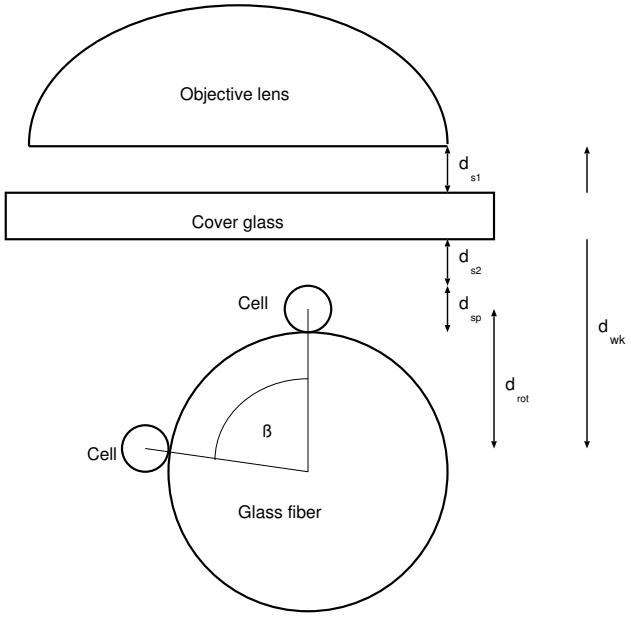

Figure 5.7: Maximal rotation angle calculation: the working distance (d_{wk}) has to be bigger or equal than the sum of the spaces above the cover glass for immersion (d_{s1}), between the coverglass and the specimen (d_{s2}), the specimen thickness (d_{sp}) and the distance added by the rotation the fiber (d_{rot}).

and the distance added by the rotation the fiber (d_{rot}) (figure 5.7):

$$d_{wk} \geq d_{s1} + d_{s2} + d_{sp} + d_{rot}.$$

The rotation distance d_{rot} depending on the fiber radius (r_f) and tilting angle β is

$$d_{rot} = \left(r_f + \frac{d_{sp}}{2} \right) (1 - \cos(\beta)),$$

which leads to a maximal availale rotation angle β of

$$\cos(\beta) \leq 1 - \frac{d_{wk} - d_{s1} - d_{s2} - d_{sp}}{r_f + \frac{d_{sp}}{2}}.$$

Assuming a space of $20\mu m$ above the cover glass for immersion fluid and another $20\mu m$ between the coverglass and the specimen leads to a maximal rotation angle of $\pm 180^\circ$ for HeLa cells and $\pm 72.5^\circ$ for mouse oocytes. Simulations of tilted image stacks showed that a tilting angle of $\pm 60^\circ$ is sufficient for reconstruction with isotropic resolution [Matula03]. This angle corresponds to a maximum object

size of 96μm. Since earlier publications [Kozubek02] the working distance of objectives has been improved significantly and is not longer a limiting factor to optical tomography. However, the depth of the focus into the specimen is still relevant for the achieved image quality and should be kept as low as possible [Hell93].

6 Measurements

A variety of measurements has already been done with the new designed micro tomographic system. Some of them are accessible for quantitative analysis, like the bead measurements (chapter 6.2) and some of them were made for descriptive presentations only, like the HeLa (chapter 6.4) and Mouse (chapter 6.5) images.

6.1 Tomograph rotation precision

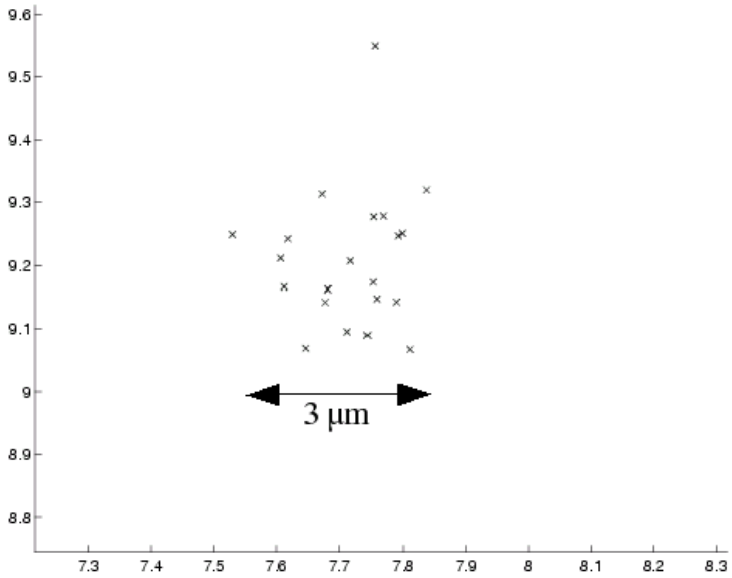

Figure 6.1: Precision of the tomograph rotation. Plotted is the y and x axis of the fiber center in 10 μm for each rotation angle during a 378° (21 steps) rotation.

To show the rotation precision 200nm beads, which were attached to the glass fiber as described in chapter 5.3, were acquired with the tomograph. Image stacks where acquired for each of the 20 rotation angles, using a 63x 1.4 oil and a 40x 0.75 air objective. Figure 6.2 shows an example with three sum images acquired at 0°, 36° and 72° rotation angle. From this bead data the rotation precision was calculated. Therefore all bead positions in the field of view where determined three

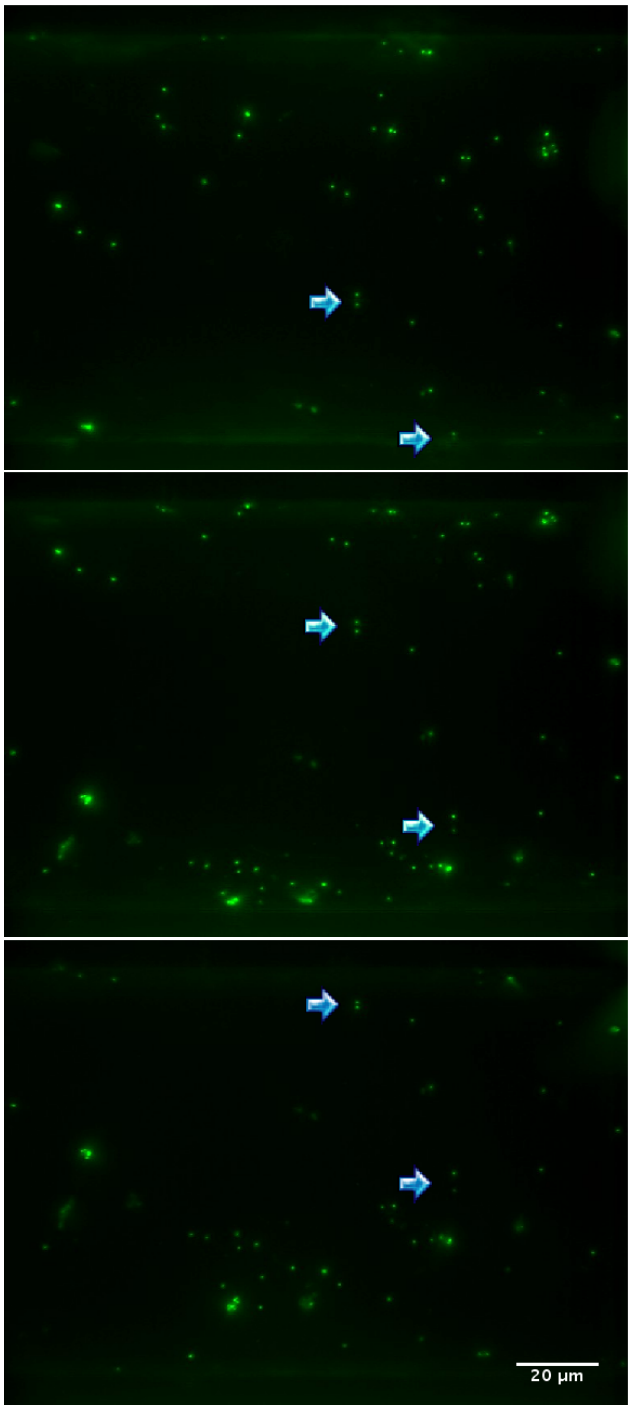

Figure 6.2: Rotation series of beads. Sum images acquired with the Heidelberg Zeiss setup, using a 40x 0.75 air objective at 0°, 36° and 72° rotation angle. The arrows point at the two bead pairs used for the distance measurements shown in figure 6.4.

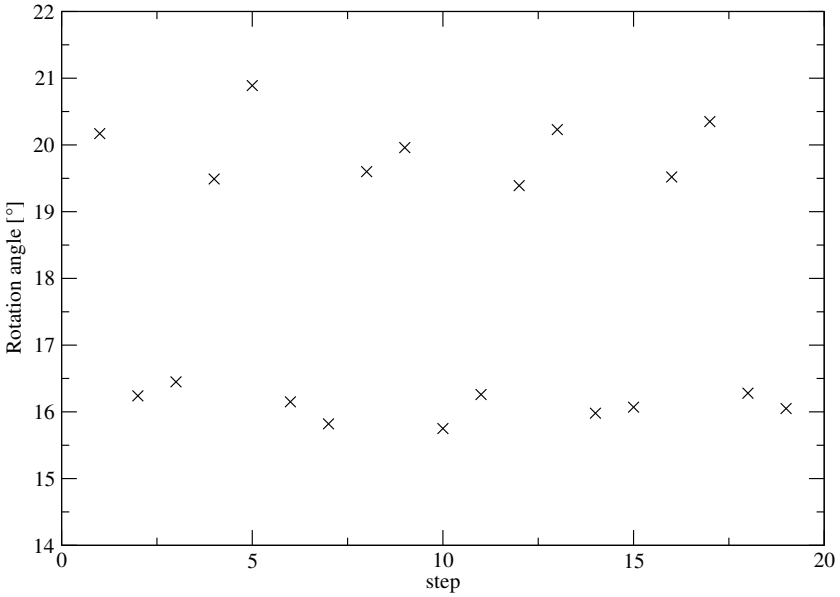

Figure 6.3: Precision of the tilting angle of the used stepper motor. Ploted is the the rotation angle vs. the number of the rotation step.

dimensional with sub pixel precision using a barycenter algorithm [Möbius27]:

$$x = \frac{\sum_{\nu \in S} \nu_x I(\nu)}{\sum_{\nu \in S} I(\nu)}, \quad y = \frac{\sum_{\nu \in S} \nu_y I(\nu)}{\sum_{\nu \in S} I(\nu)}, \quad z = \frac{\sum_{\nu \in S} \nu_z I(\nu)}{\sum_{\nu \in S} I(\nu)}$$

where x, y and z are coordinates of the centroid, S is the set of voxels, which are determined by the segmentation algorithm, that belong to the object, ν_x, ν_y and ν_z are the x, y, and z-coordinates of the voxel ν, and $I(\nu)$ is the intensity of the voxel ν. Within one image a set of such points exists and can be used for image alignment.

Afterwards a circle was fitted in the y-z plane through all of them and for every rotation angle. Figure 6.1 shows the y and z axis of the fiber center for each of these circles during a 378° (21 steps) rotation. The lateral and axial movement of the fiber was measured to be below $3\mu m$ during this rotation which corresponds to the small observed movement during tilting. Related to a visible fiber length of $2000\mu m$ between the two fiber bearings this corresponds to a lateral movement of 0.15%.

The precision of the tilting angle was also measured from the bead images using a weighted bipartite graph [Chartrand85] where the optimum transformation function was computed in a least squares manner based on the coordinates of the centres of gravity of the matched objects [Matula03]. The results in figure 6.3

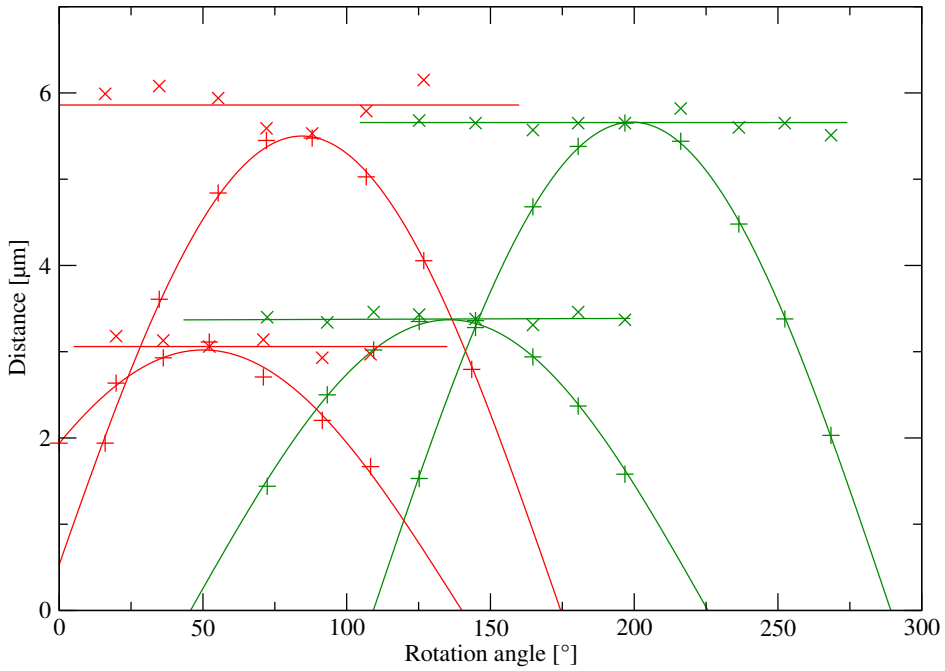

Figure 6.4: Plot of the measured distance vs. rotation angle. The lines are average 3 dimensional distances measured from image stacks for each rotation angle (x). The sinus curves are fits of the 2 dimensional projections of the distance in the lateral plane (+) with the true distance as maximum. Shown are measurements with a 40x 0.75 (green) and a 63x 1.4 (red) objective.

show that the angle is not 18° ±1° as described by the stepper motor manufacturer, but a mixture of 16° and 20° steps in a way that two 16° steps are followed by two 20° steps. However, this does not influence the planned image fusion, because the rotation angle has to be measured for the precise image alignment anyway.

6.2 Distance measurements

The major advantages of micro axial tomography is it's high resolution in all three dimensions. To show this advantage distances between the 200nm beads were measured with the tomograph. The arrows shown in figure 6.2 point at the two bead pairs used for the distance measurement. The bead positions were measured in the image stack with sub pixel (nm) precision using a center of gravity algorithm. The precise rotation angle was measured using a weighted bipartite graph where the optimum transformation function was computed in a least squares manner based on the coordinates of the centres of gravity of the matched objects

[Matula03].

To show the precision enhancement the distance was calculated in two ways: first the distance was calculated "as usual" in microscopy from all three dimensions of the image stack.

$$d = \sqrt{(x_1 - x_2)^2 + (y_1 - y_2)^2 + (z_1 - z_2)^2}$$

This formula includes the low resolution optical axis of the microscope (z). The tomographic approach is only to use the high resolution lateral axes (x,y) projection $d_{project}$ of the distance:

$$d_{project} = \sqrt{(x_1 - x_2)^2 + (y_1 - y_2)^2}.$$

Both measurements were done for each rotation angle. The first results in 8 to 9 different distances depending on the number of acquired rotaton angels (horizontal line in figure 6.4) from which the median and standard deviation were calculated. The second measurement results in a sinus curve with the true distance d_{true} as the maximum and $\Delta\varphi$ as offset of the rotation angle:

$$d_{project}(\varphi) = d_{true} \cdot \sin(\varphi + \Delta\varphi).$$

This formula was used for a Marquardt-Levenberg least squares fit with the maximum distance and offset as parameters, which gives the real distance and a standard deviation to this value. The measured tomographic and 3d distances are shown in table 6.1.

Objective	$d_{tomographic}[\mu m]$	$d_{3d}[\mu m]$
40x	(3.37 ± 0.02)	(3.41 ± 0.07)
0.75	(5.66 ± 0.01)	(5.64 ± 0.08)
63x	(5.50 ± 0.03)	(5.87 ± 0.25)
1.4	(3.03 ± 0.04)	(3.06 ± 0.09)

Table 6.1: Measured bead distances (four pairs) tomographic and 3d with different objectives.

6.3 Microscope stage drift

During the first measurements with the new Zeiss Axioplan 2 imaging microscope at Bar Harbor large movements of the stage during image stack acquisitions were detected. The stability of the microscope stage is very important for the acquisition of large specimen, e.g. mouse oocytes, which takes a long time because of the high

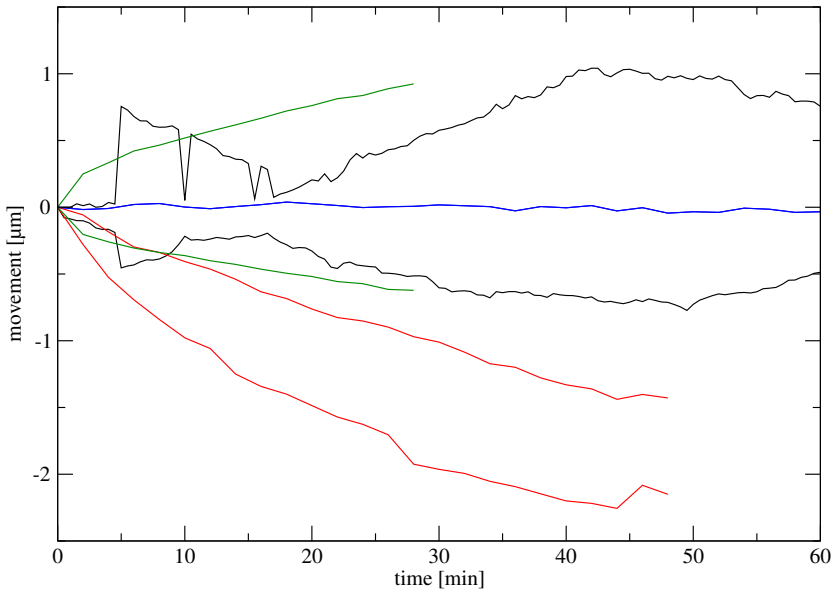

Figure 6.5: Comparison of microscope stage drifts. Zeiss Axioplan Setup at Bar Harbor (black), Heidelberg (red), Leica DMRB (green) and Zeiss Standard 25 (blue).

number of slices. During the acquisition time of one image stack (30 to 60 min) the microscope stage has to be stable in x and y direction to allow image analysis like deconvolution or image fusion.

To measure the stage movements time series without axial movement of the stage were acquired. To quantify the speed and distance of the movement the acquired image stacks were analyzed with a cross correlation algorithm implemented in Matlab. During a period of 60 minutes the microscope has moved $1\mu m$ before properly adjusting the microscope room air condition which caused temperature changes larger than 5° Celsius. Afterwards the temperature was stable within about 1° Celsius and the movement was reduced to $0.5\mu m$. This drift was seen in all image stacks acquired with the Axioplan microscope and made it necessary to align all images with special softare algorithms (chapter 7.1). Even larger movements were seen with the same microscope setup installed at the German cancer research center, which was used for comparative measurements. Also the Leica DMRB microscope at Heidelberg showed quite a large drift, while the old Zeiss Standard 25 setup was the most stable in our experiments (figure 6.5) [Reinhard04].

6.4 HeLa cells

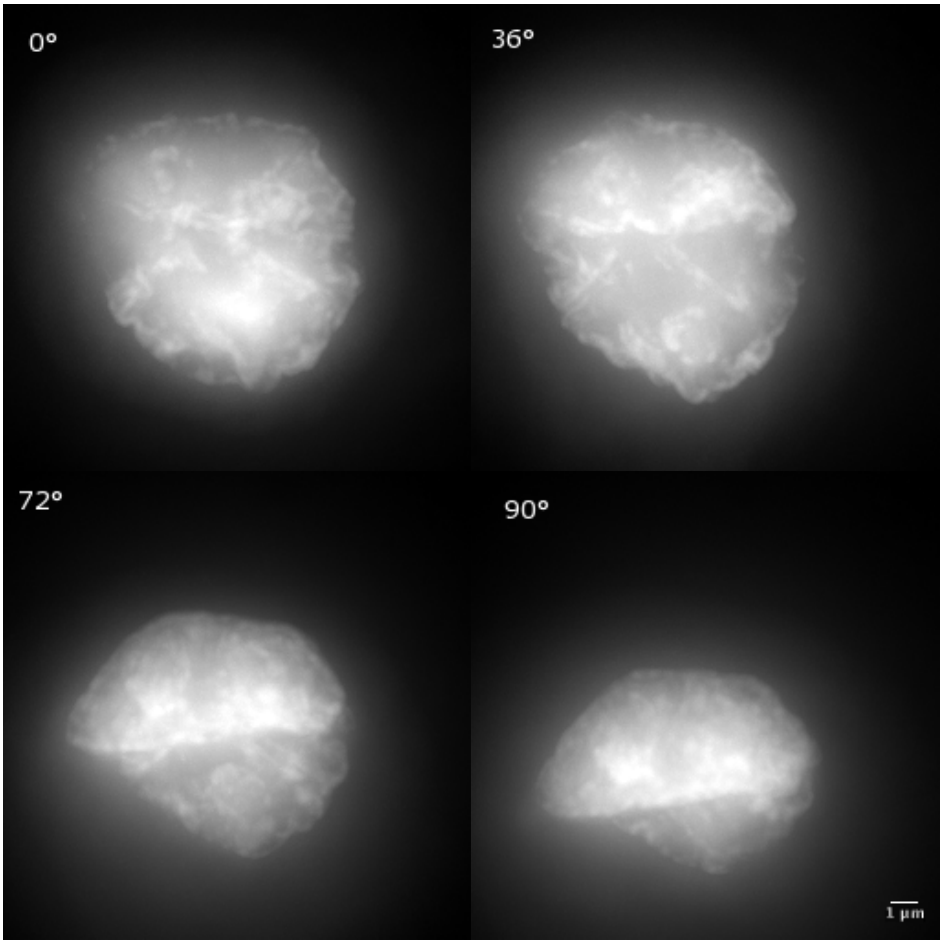

Figure 6.6: Rotation series of a single DAPI stained HeLa cell. Sum images of the different rotation angel (0°, 36°, 72° and 90°) image stacks acquired with a 100x 1.4 oil objective. The bright areas of the images correspond to high A-T density regions of the cell nucleus

For this experiment HeLa cells were fixed with formaldehyde, stained with 4',6-Diamidino-2-phenylindole (DAPI) and then attached to the glass fiber. Figure 6.6 shows sum images of the stacks acquired in a rotation series with a 100x 1.4 oil objective at the Bar Harbor Zeiss setup. The DAPI stain binds to the minor groove of the DNA helix around Adenin Thymin clusters, which increases the amount of fluorescence twenty fold. Therefore the bright areas of the images correspond to high A-T density regions of the cell nucleus. Figures 6.6 and 6.7 show the original data from the microscope camera. Several different deconvolution programs were compared with these data stacks (chapter 7.2).

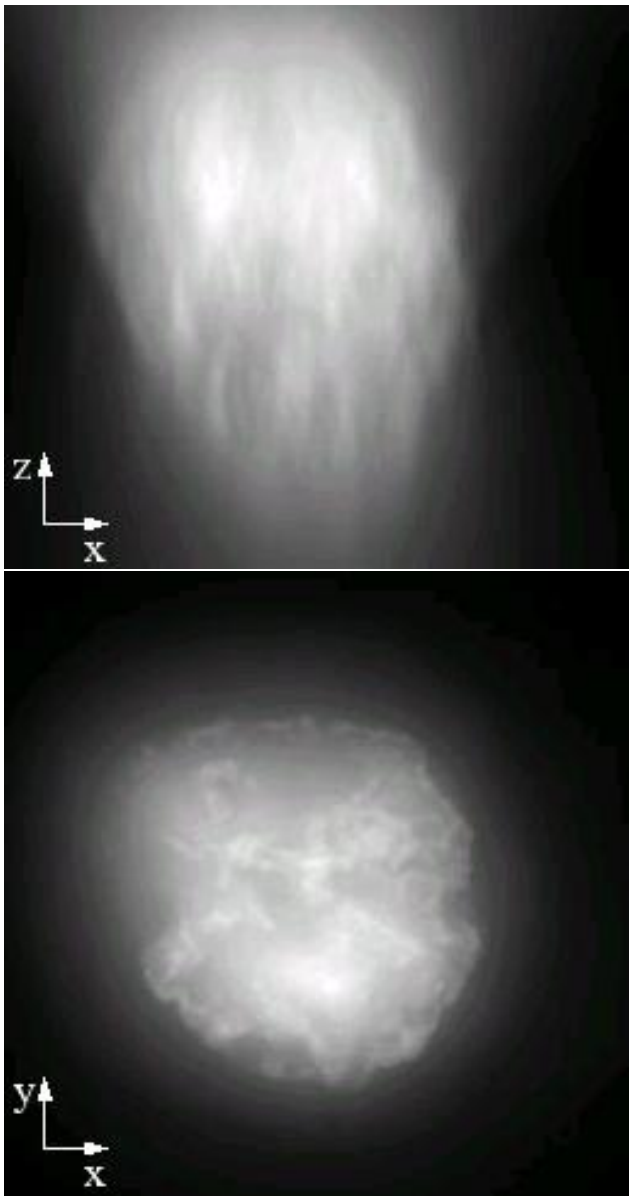

Figure 6.7: Top: the last rotation angle of figure 6.6 which was rotated by software so that the xz plane is visible. The low axial resolution of epifluorescence microscopy is easily visible. Bottom: the first rotation angle of figure 6.6. The rotation has now been done with the tomograph hardware instead of software. Both image axes are now shown in the high lateral resolution

6.5 Mouse oocytes

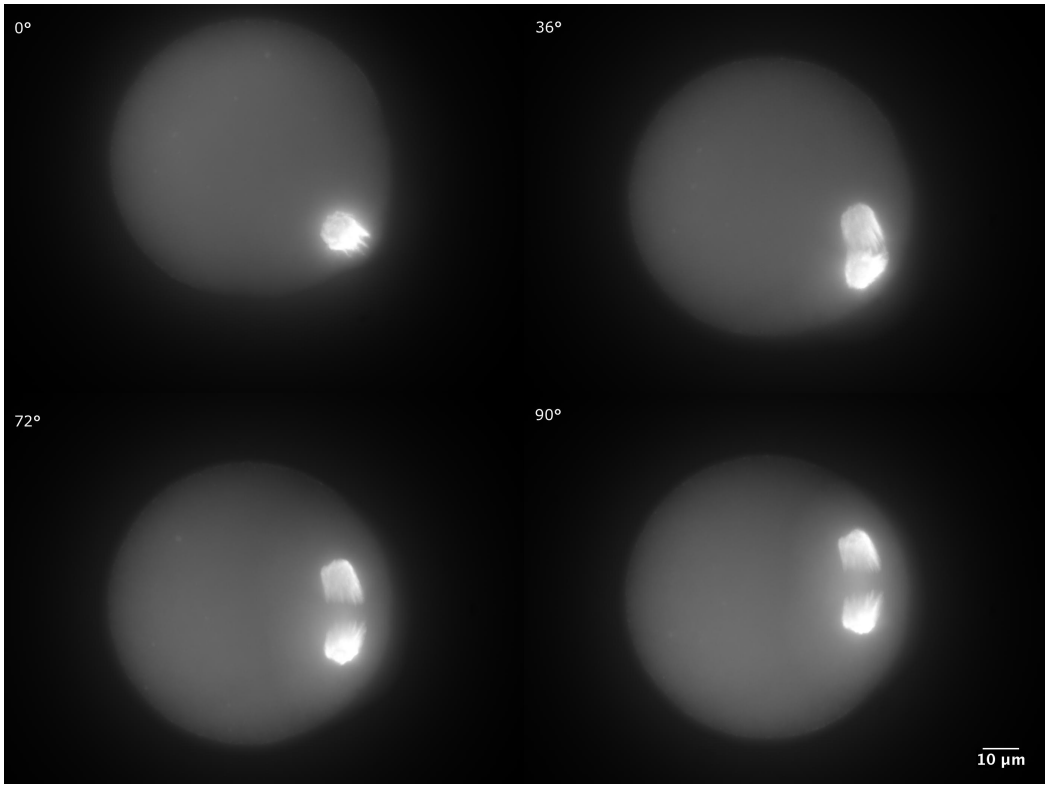

Figure 6.8: Rotation series of a single mouse Oocyte, sum images of image stacks acquired at 0°, 36°, 72° and 90° rotation angle with a 63x 1.4 oil objective at the Bar Harbor Zeiss setup. The oorcytes were fixed during the first cell division and the spindle apparatus had been stained with rabbit TACC3 protein antibodies.

Mouse oocytes are much bigger than the cells normally used. As a proof of concept they where acquired with the tomograph as well. The thickness of the fiber ($125\mu m$) and the oocytes ($80\mu m$ on all sides of the fiber) is $285\mu m$ while the typical cover glass thickness is $170\mu m$. The system was therefore equipped with normal object slides with a thickness of $1mm$ as spacer between cover glass and object slide (chapter 5.5). Figure 6.8 and figure 6.11 show sum images of image stacks acquired at 0°, 36°, 72° and 90° rotation angle with a 63x 1.4 oil objective at the Bar Harbor Zeiss setup. Again the original microscope images are shown without any image manipulation. The oocytes were fixed during the first cell division and the spindle apparatus was stained with rabbit TACC3 protein antibodies.

Figure 6.9 shows a cut of the first rotation angle of Figure 6.8 (upper part) which was rotated by software so that the xz plane is visible. The low axial resolution of

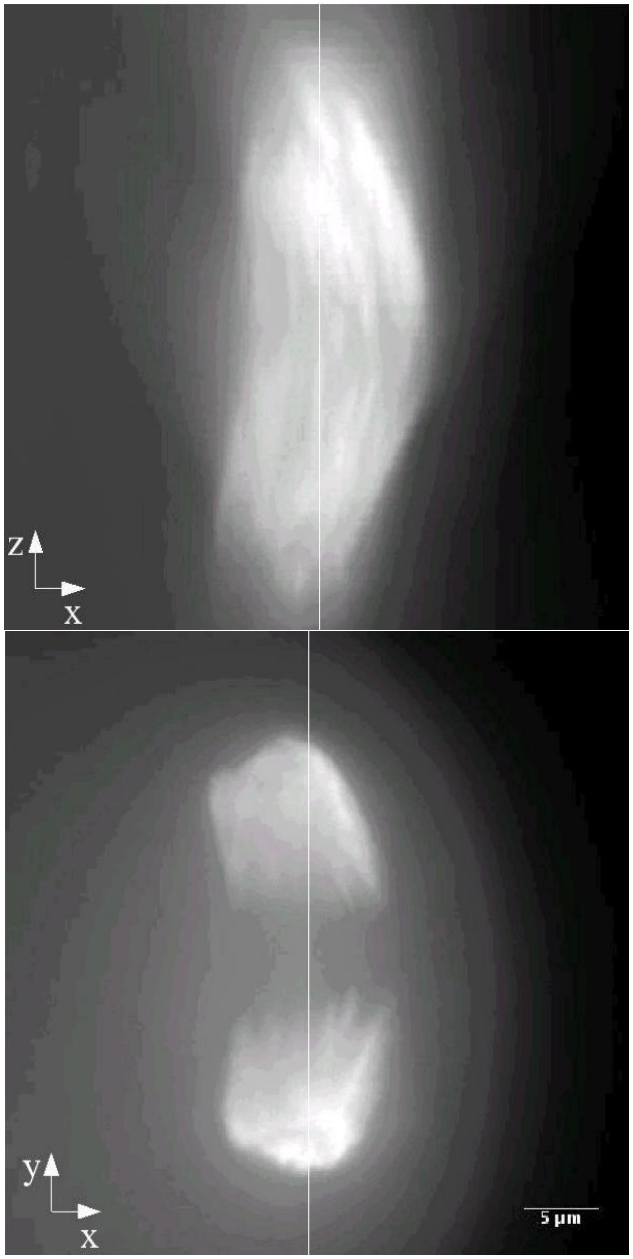

Figure 6.9: Top: the first rotation angle of figure 6.8 which was rotated by software so that the xz plane is visible. The low axial resolution of widefield epifluorescence microscopy is easily visible. Bottom: a cut of the last rotation angle of figure 6.8. The rotation has now been done with the tomograph hardware instead of software. Both image axes are now shown in the high lateral resolution. The white lines are shown as linescans in figure 6.10.

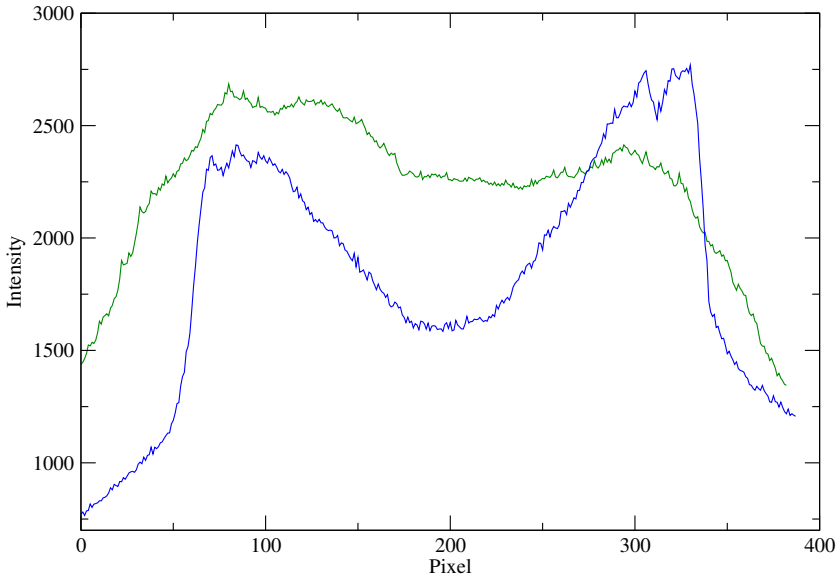

Figure 6.10: Vertical linescans of the two oocyte images in figure 6.9. Axial (green) and lateral (blue) resolution. The lateral linescan shows two clearly separable maxima (both spindel apparati), where the axial scan shows only one large object.

the system is easily visible. The lower part shows a cut of the last rotation angle of figure 6.8. The rotation has now been done with the tomograph hardware instead of software rotation. Both image axis are now shown in the high lateral resolution.

Figure 6.10 shows vertical linescans from both images in figure 6.9 in which the axial and lateral resolution is easily to distinguish. The lateral resolution shows two clearly separable maxima (both spindle apparati), where the axial scan shows only one large object. In image analysis the segmentation software would be able to separate both spindel apparati with the lateral resolution, but not with the axial resolution.

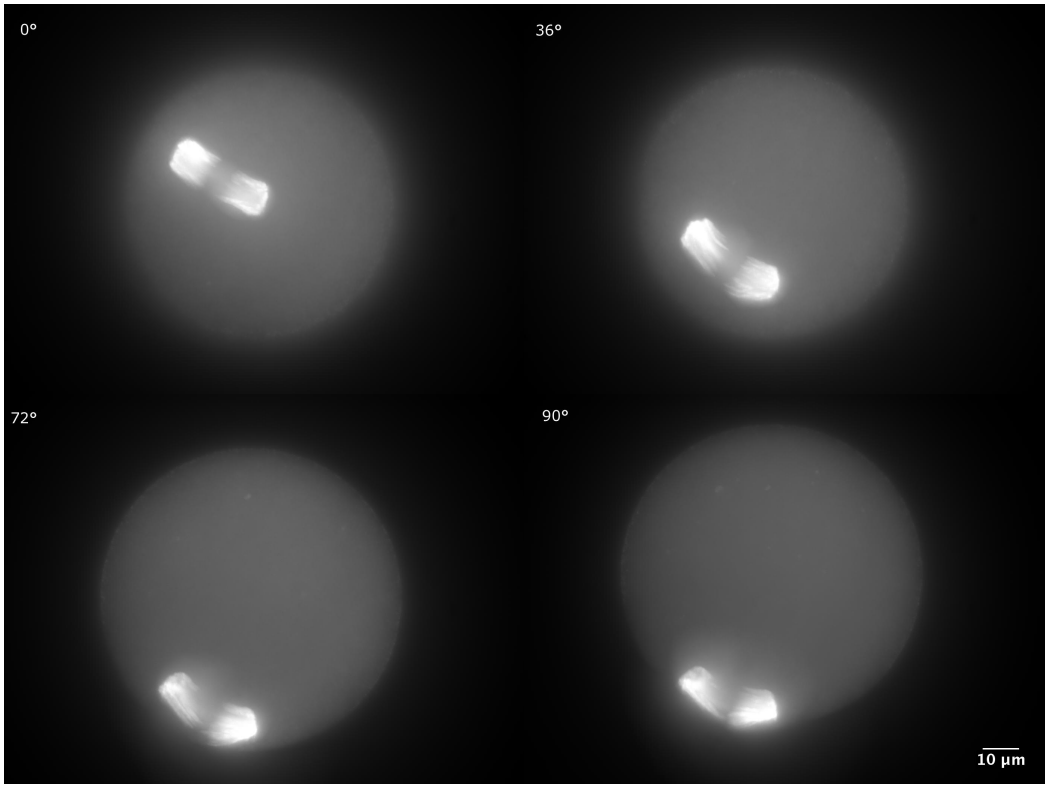

Figure 6.11: Rotation series of a single mouse Oocyte, sum images of image stacks acquired at 0°, 36°, 72° and 90° rotation angle with a 63x 1.4 oil objective at the Bar Harbor Zeiss setup. The oocytes were fixed during the first cell division and the spindle apparatus was stained with rabbit TACC3 protein antibodies.

7 Image reconstruction

7.1 Correction of microscope stage movement

For a accurate deconvolution the PSF of the used microscope is needed. During PSF acquisition a significant lateral and axial movement of the microscope stage was observed (about one μm), which was caused by temperature changes in the microscope room and general instability of the Zeiss setup (Measurements with a similar Zeiss setup at the German cancer research center showed a movement of two μm). Therefore the PSF had to be aligned, which was done with the Khoros

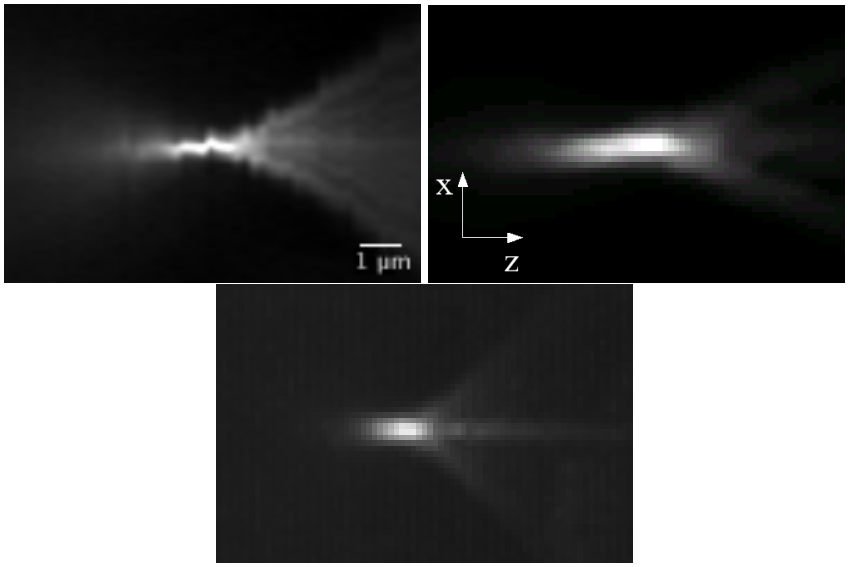

Figure 7.1: Measurements of the PSF: Movement of the stage at the Heidelberg and Bar Harbor Zeiss setup. Sum images of a 200nm bead in x and z direction with (right) and without (left) alignment at the Bar Harbor (top) and Heidelberg (bottom) setup.

software package. Figure 7.1 shows the PSF before and after the software alignment process. Of course, the acquired image stacks of biological specimen had to be aligned as well. The improvement of deconvolution with the aligned image stacks is shown in figure 7.2.

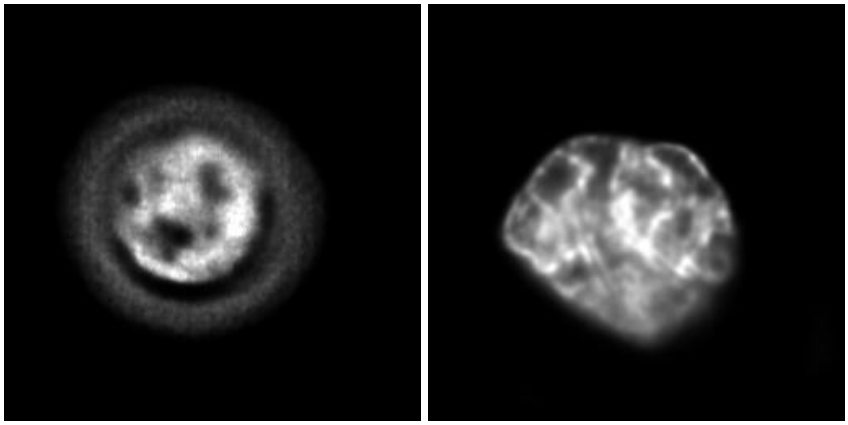

Figure 7.2: Khoros based deconvolution of the HeLa cell image stack (figure 6.6) with (right) and without (left) image alignment.

7.2 Comparison of deconvolution algorithms

To show and compare the possibilities of digital image reconstruction (chapter 4) one of the HeLa cell image stacks (figure 6.6) was analyzed with several different deconvolution packages available to our lab. Most of these programs are based on maximum likelihood algorithms (chapter 4.2) with different parameters and combined with digital filters.

All figures show one selected plane of the image stack on the left and a sum image of the rotated image stack on the right. Figure 7.3 shows the original image on top, as well as deconvolution with the Huygens software package [SVI] and a maximum likelihood based algorithm developed in [Heintzmann99] and implemented in Khoros. Figure 7.4 shows deconvolution with a Tikhonov algorithm developed in [Kryvanos05], another maximum likelihood algorithm implemented in matlab, and a simple high pass filter based on fourier transformation and implemented in Khoros.

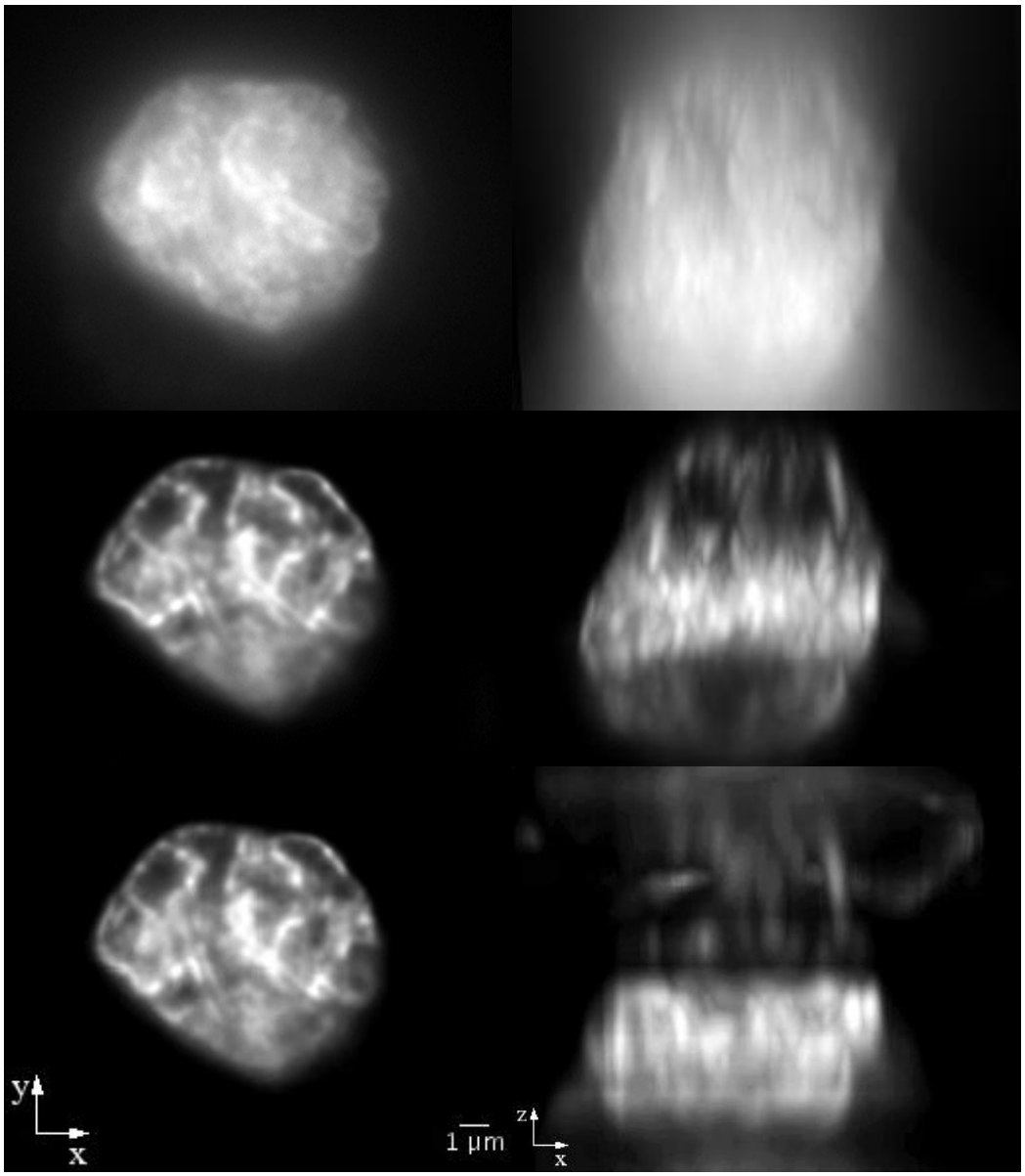

Figure 7.3: HeLa cell image stack (figure 6.6) original (top) and deconvolved with with the Huygens (middle) and Heintzmann (bottom) implementations of a ML algorithm. Shown is the lateral (left) as well as the axial (right) direction.

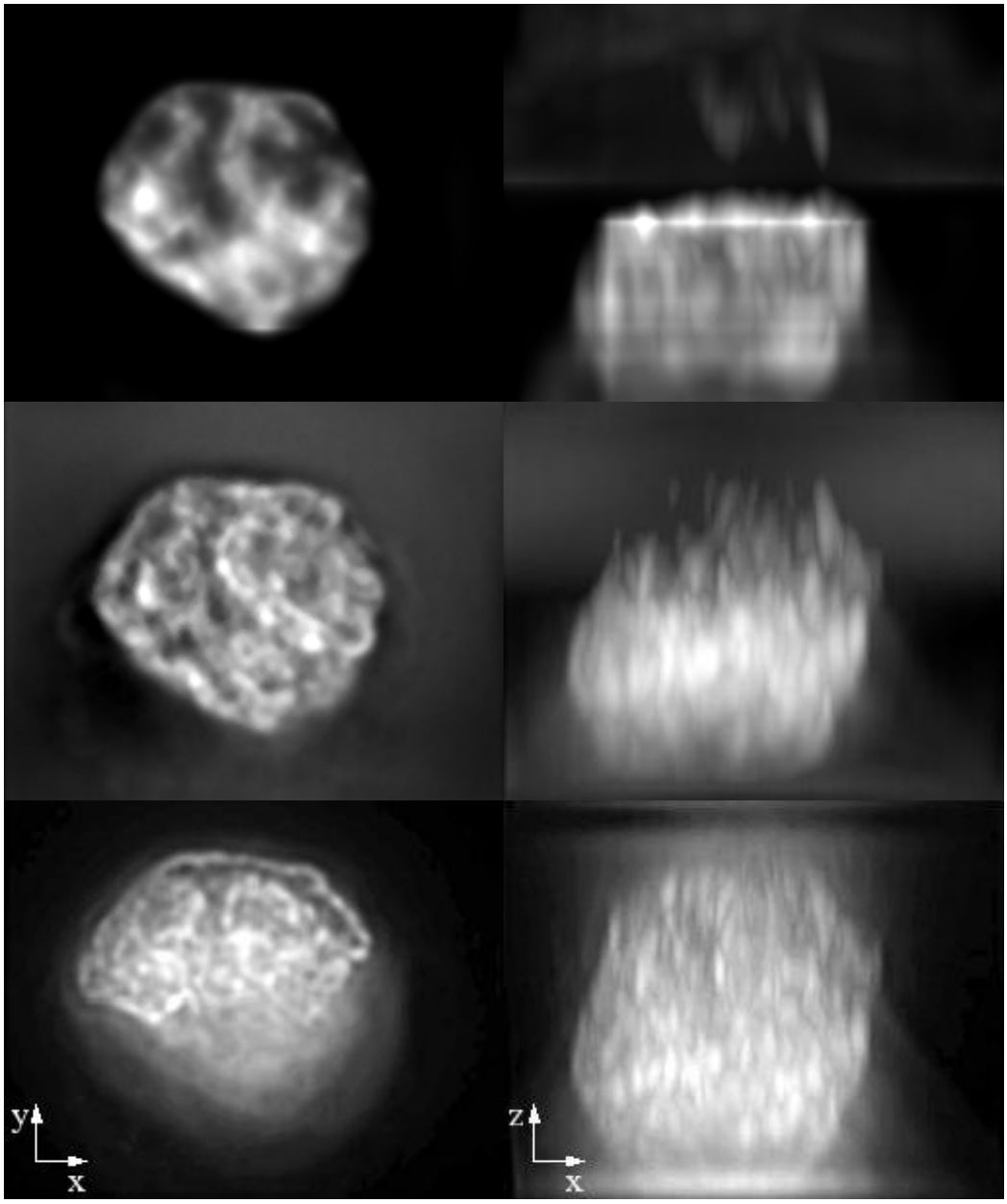

Figure 7.4: HeLa cell image stack (figure 6.6) deconvolved with a Tikhonov (top) and a ML (middle) algorithm implemented in matlab, and a simple high pass filter (bottom) implemented in Khoros. Shown is the lateral (left) as well as the axial (right) direction.

7.3 Deconvolution of HeLa cells

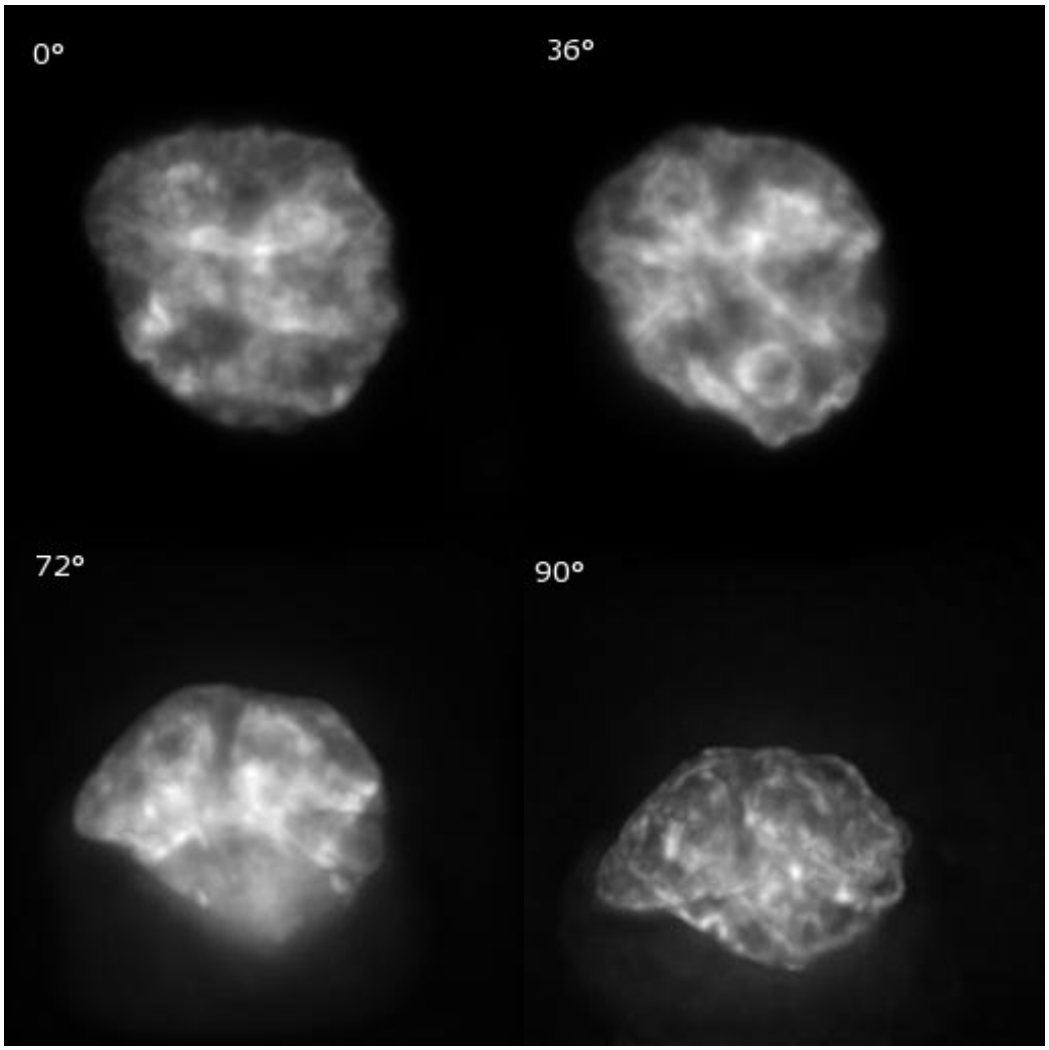

Figure 7.5: Deconvoluon of HeLa cell rotation series (0°, 36°, 72° and 90°) in figure 6.6 on page 42 which were deconvolved with the Huygens software package.

The comparison of deconvolution algorithms showed the best quantitative results with the Huygens software package. Therefore all of the following deconvolutions were done with this program, which is based on a maximum likelihood algorithm and using a simulated PSF. Figure 7.5 shows maximum images of the deconvolved image stacks of the HeLa cell rotation series in figure 6.6 on page 42. After deconvolution, the out of focus blur is minimized significantly, as expected.

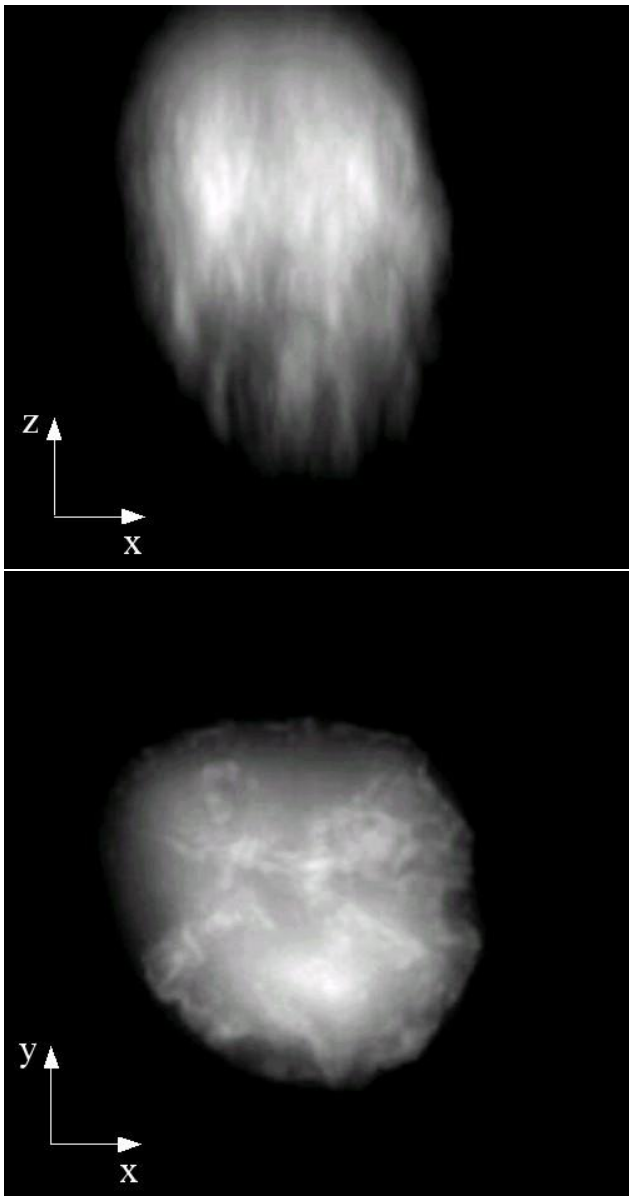

Figure 7.6: Top: the last rotation angle of figure 7.5 which was rotated by software so that the xz plane is visible. The low axial resolution of epifluorescence microscopy is easily visible. Bottom: the first rotation angle of figure 7.5. The rotation has now been done with the tomograph hardware instead of software. Both image axes are now shown in the high lateral resolution

7.4 Deconvolution of mouse oocytes

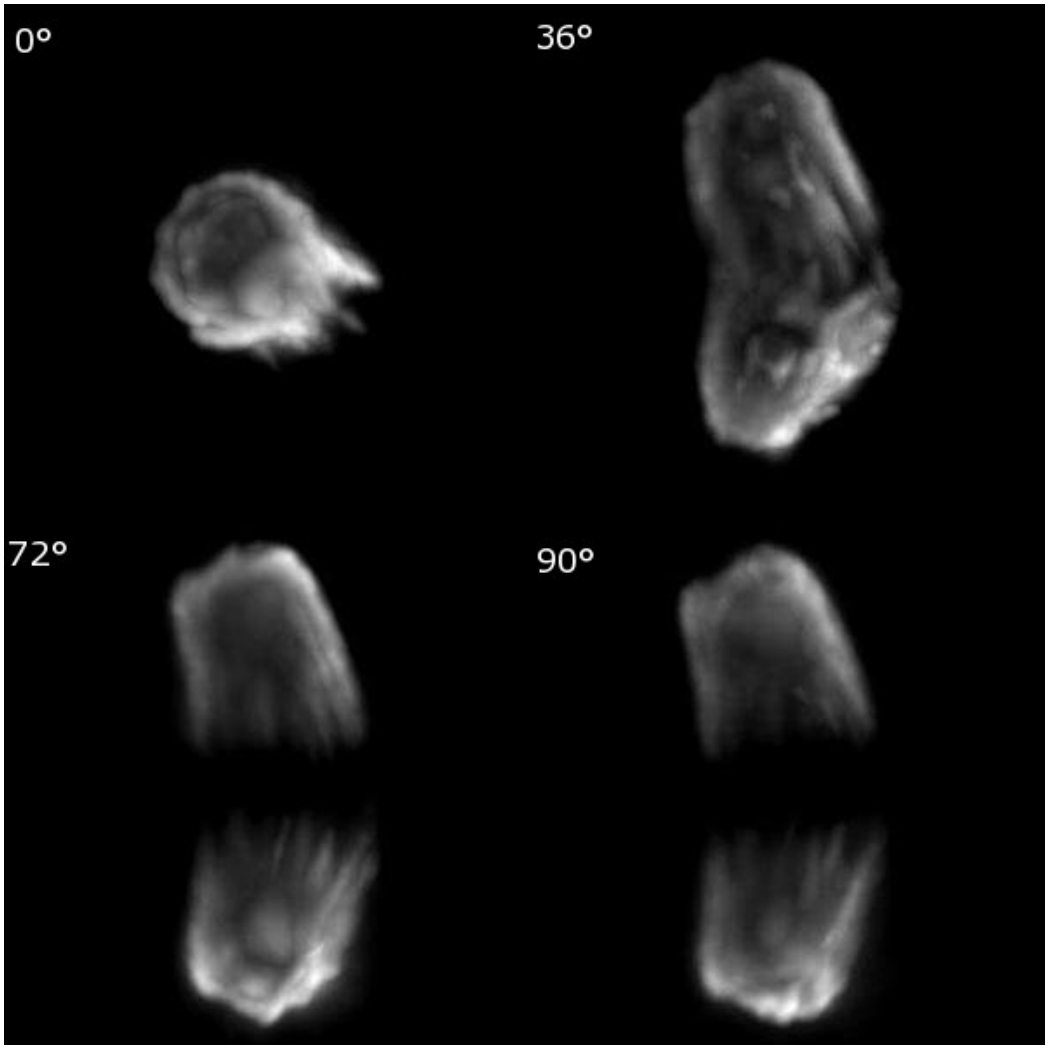

Figure 7.7: Deconvoluon of mouse oocytes. Cuts from the rotation series (0°, 36°, 72° and 90°) in figure 6.8 on page 44 which were deconvolved with the Huygens software package.

The complete mouse oocyte image stacks could not be deconvolved because of their size (1 Gigabyte per stack). Therefore the spindle apparatus region, which is much smaller than the whole nucleus, was cut and deconvolved with Huygens. Figure 7.7 shows intensity projection images of these cut and deconvolved image stacks of the mouse oocytes from figure 6.8 on page 44 for all acquired rotation angles (0°, 36°, 72° and 90°).

7.5 Stereo volume rendering

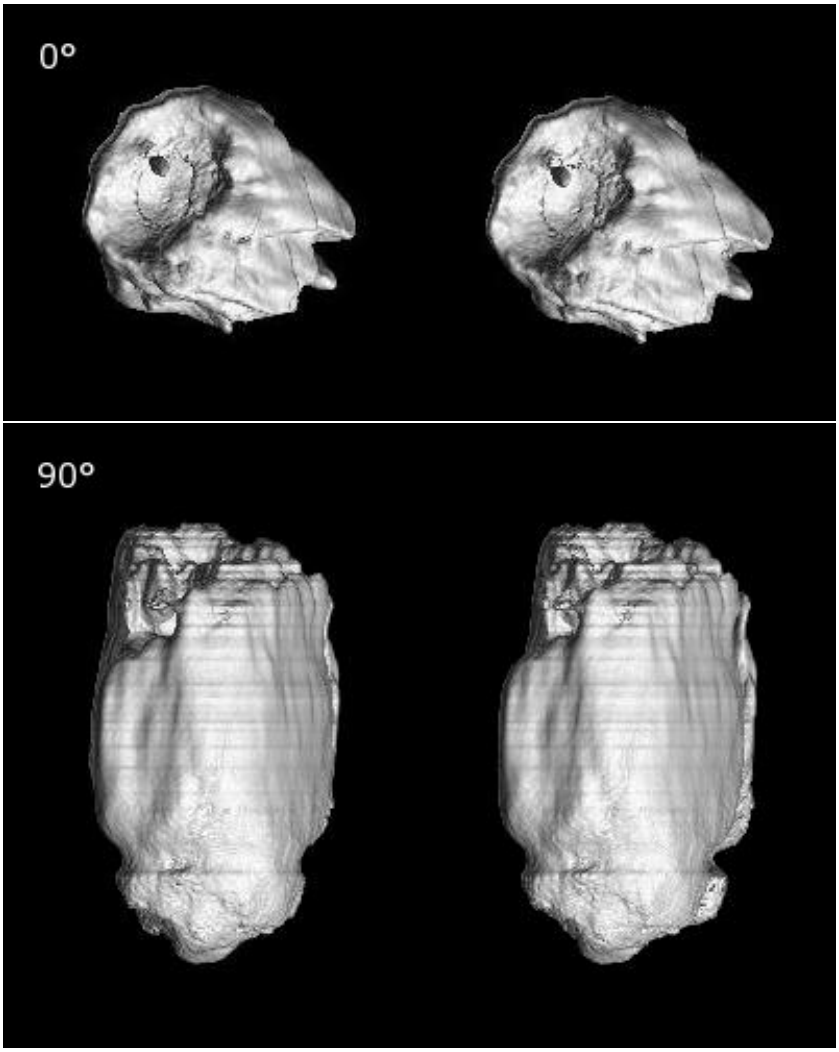

Figure 7.8: Stereo volume rendering of mouse oocytes. Cuts from the 0° (top) and 90° (bottom) rotation angles in figure 7.7. The bottom image was rotated by 90° with software.

The deconvolved images were now processed with a raytrace volume rendering algorithm developed by [Abràmoff]. Figures 7.8 and 7.9 show comparisons of stereo volume renderings of the deconvolved image stacks in figure 7.7 at 0° and the 90° rotation angle where the top images shows tomographic rotation and the bottom image rotation done with software. To see the stereo effect, you have to align these images horizontally, put your eyes about 10-20" (25-50 cm) from the image and gaze into infinity between them.

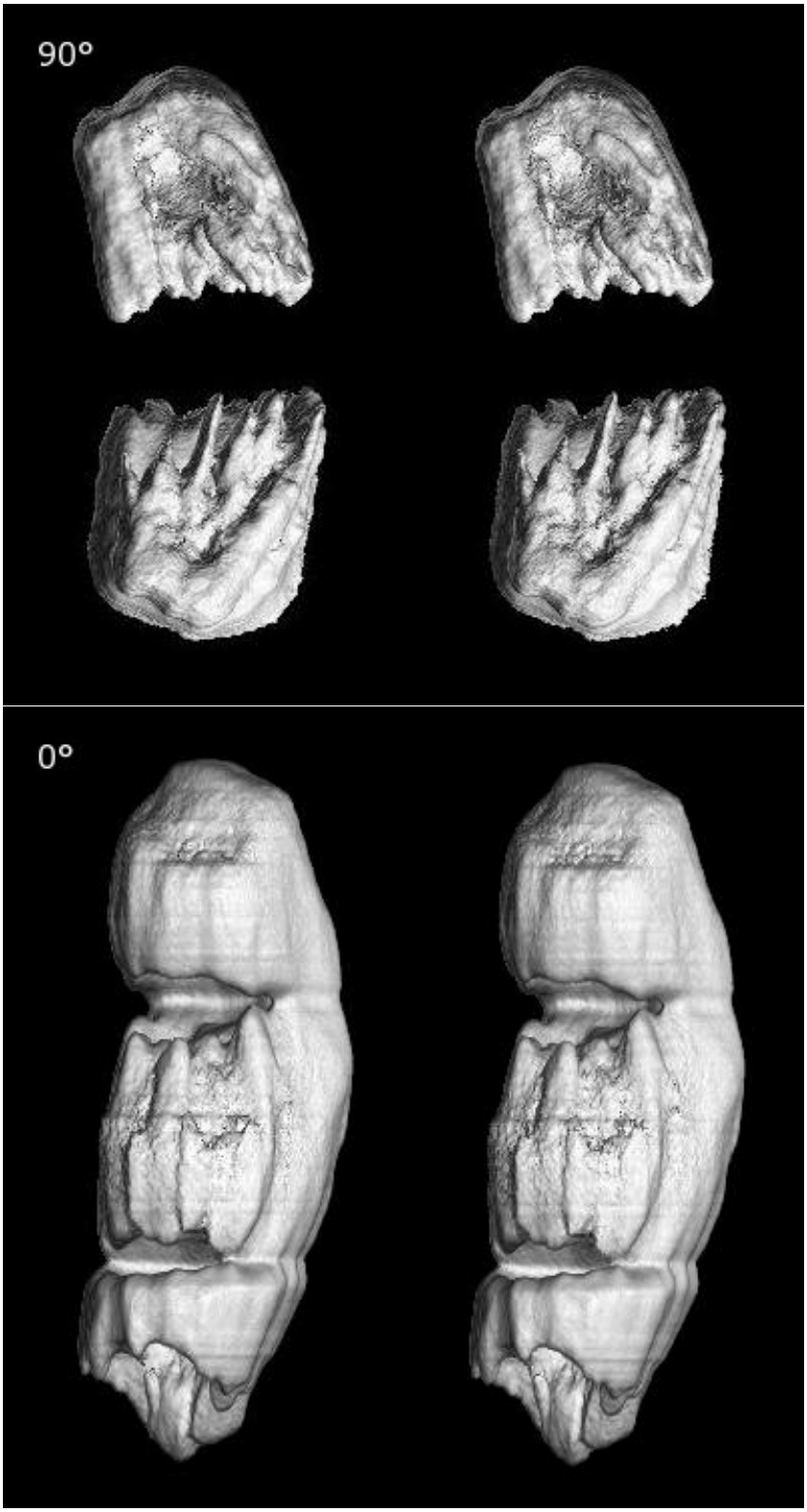

Figure 7.9: Stereo volume rendering of mouse oocytes. Cuts from the 90° (top) and 0° (bottom) rotation angles in figure 7.7. The bottom image was rotated by 90° with software.

8 Discussion and summary

The aim of this thesis was to implement a recently developed micro axial tomograph to different microscope systems for measurements with thin specimen (HeLa) and thick specimen (oocytes) as well as to show the usability and precision of the system. Therefore a surface treatment procedure to attach beads, as well as biological specimen of different size, to the fiber was developed. All measurements presented in this thesis are based on the fiber preparation shown in appendix A which is quite robust and easy to handle.

Measurements with fluorescent beads showed the huge gain in distance measurement precision. With the 40x 0.75 air objective the distances were distinguished up to eight times more precisely as compared to standard wide field microscopy. The measurements with the 63x 1.4 oil objective are slightly below this precision, which might be caused by the high numerical aperture, allowing abberated light which passed through the glass fiber to be gathered by the objective, because of the high objective angle. A simulation of the light path, which should be done in the near future, might show whether this problem occurs. It could, however, be solved with refractive index matching of the glass fiber and it's surrounding medium.

Measurements of the rotation precision showed the high precision of the fiber bearings and the setup. The lateral and axial movement is below $3\mu m$ during a 360° rotation. This high precision enables the system to acquire a whole rotation series automatically, and without readjusting the stage after each tilt, while the small shift is corrected by software.

The precision of the stepper motor rotation angle is not as good as expected, but it has to be computed preciseley from the acquired images for exact image alignment anyway, so this is no significant problem for the system.

An important use of the beads in acquired image stacks is their function as reference points for image alignment, which has to be done before image fusion. If there are not enough reference points inside the cells (e.g. Fish spots), beads can be attached to the fiber beside the cells, and be used as reference objects. First experiments have been done to show this possibility.

Movements of the Bar Harbor microscope stage resulted in difficulties with the deconvolution algorithms. They were first minimized by improving the temperature stability of the microscope room with adjustments of the air condition in

collaboration with the local engineers. But the movement was still easily visible in acquired image stacks. Second the microscope setup was part by part changed to find the movement's reasons, but unfortunateley this did not help to solve the problem. Finally the movement was accepted as being part of this microscope series, which was proven by measurements with the same setup at a different location. Recently Zeiss admitted to know about this problems and developed a new microscop stand. To be able to use the microscope, different alignment algorithms where tested which improved the image quality significant, and made deconvolution possible.

Using biological specimen which are very different in size made it necessary to adapt the spacing glasses of the tomograph. Calculations of the maximal rotation angle in dependence of the object size where done to find the object size limitations of the currently used setup. Afterwards specifications to handle objects with sizes between $0.2\mu m$ and $100\mu m$ were developed and their functionality was shown in experiments. Furthermore the tomograph was adapted to different embedding media e.g. glycerol or phosphate buffered saline (PBS).

The HeLa cell images, as well a the mouse oocytes, show a biological applications of micro fluorescence tomography. Not only images of small cells like HeLa's but also large embryos could be acquired tomographicaly. The spindle apparatus images clearly show the advantages of axial tomography. With the newly developed system it is possible to acquire additional information about the object which is usually not accessible to image analysis. Quantitative image analysis with automated image segmentation would be able to separate both spindel apparati only with micro fluorescent tomography, which shows the opportunities of the technology, as planned for this thesis.

The comparison of different deconvolution algorithms identified Huygens as the program which works best with our image stacks. The out of focus blur was reduced significantly, more details are visible after deconvolution. The disadvantage is that some artifacts are visible in the deconvolved images which are most probably caused by mismatch of the refractive index. Another reason is the use of an oil objective while the specimen where embedded in PBS, which has a refractive index close to water. A solution for this would be the usage of water objectives which have the additional advantage of a higher working distance. First experiments with such an objective were done and showed the advantages clearly. Unfortunateley the first objective provided by Zeiss had lots of uncorrected abberations and Zeiss was not able to deliver a working one in time.

A new Fish protocol (appendix B) was developed to stain specific gene regions in cell nuclei attached to glass fibers. First experiments showed, that the protocol

is already working, but the camera at the Heidelberg Zeiss setup was not sensitive enough to detect them. However, the spots could be detected with a confocal microscope, and the tomograph system is now adapted to a Leica microscope with a camera sensitive enough to acquire these spots. So in the near future tomographic measurements of FisH stained cells will be possible at Heidelberg.

An important future perspective is to develop an algorithm to merge the different tilted image stacks to one image with improved isotropic resolution. This would make high resolution 3D tomographic images accessible for automated quantitative image analysis with the optimum precision that can be obtained by a given microscope setup. Some algorithms, like tilted view maximum likleyhood, a statistical approach and fourier space model fusion, are already implemented and tested for some special datasets but, so far, none of them works with all kinds of wide field microscope data sets. However the experiments show, that the best results are expected with a fourier space based model fusion algorithm. As a next step this algorithm has to be implemented. This has most probably to be a parallel implementation to cope with the large stacks (about one gigabyte per rotation angle) acquired of mouse oocytes.

The micro axial tomograph system is now easily usable for a variety of biological applications with several wide field microscopes. Depending on the specimen used and their embedding medium different preparation procedures which were developed in this thesis can be used to adapt the tomograph.

A next step could be to adapt the tomograph to other types of microscopes with non isotropic resolution like spatially modulated illumination (SMI) microscopes [Failla03].

A Preparation of glass fibers

Storage of fibers in 50% H_2O + 25% Isopropanol + 25% Ammonia(50%)

- Wash in 50% H_2O + 25% Isopropanol + 25% Ammonia(50%) for one minute.
- Wash in clean H_2O for one minute.
- Store in $0,1\%$ (3-Aminopropyl)trimethoxysilane (Sigma 09326) in abs. EtOH for 30min.
- Store in glutaric dialdehyde-gas (Glutaraldehyde 50% in H_2O for 30min.
- Store in 1% Poly(ethylenimin) (Sigma P-3143) in H_2O for 30min.
- Store in specimen suspension for 30min.
- Wash in clean H_2O for one minute.

B Codenaturation FisH protocol for cells attached to glass fibers

Buffers	2xSSC + NP-40	100	*ml* 20xSSC
		900	*ml* H_2O
		1	*ml* NP-40
	Triton	1.4	*ml* 0.7% Triton
		0.2	*g* Saponin
		198.6	*ml* 2xSSC
	Hybridmix	7	μl Hybridization buffer
		1	μl Sonden
		2	μl H_2O

Procedure

attach fixed cells to fibers
stain with 0.5 $\mu g/ml$ DAPI
wash with 2xSSC
incubate with 37 $\mu g/ml$ Salomon sperm DNA
wash with 2xSSC
store 30 min in Triton buffer
wash 2x 5 min in 2xSSC
add hybridization mix and cover
denaturate 5 min at 75C
store over night in humidified box at 37C

wash for 5 min in 2xSSC + NP 40
dry

C C++ program to rotate the fiber

```
onestep.cpp : Defines the entry point for the console
application.

#include "stdafx.h"
#include "ioDL.h"
#include <stdlib.h>
#include <iostream>
#include <Windows.h>

using namespace std;

//use LPT1 if no other port given
#define DEF_PORT 0x378

//Definitions of what we consider sending a one
// zero to the stepper controler should be
//Useful to change for different pinouts, signal polarities etc...
#define SIG_HIGH 0x1
#define SIG_LOW 0x0

/*Duration of various stages of the pulse in milliseconds
NB - not exact, due to use of sleep.

  LOW_TIME_1    HIGH_TIME    LOW_TIME_2
              |------------|
 |------------|            |-----------|

*/
#define LOW_TIME_1 10
#define HIGH_TIME 10
#define LOW_TIME_2 0

int _tmain(int argc, _TCHAR* argv[])
{
unsigned int port = DEF_PORT;
```

```
//Check to see if we got an alternative value for port
//on the command line
if (argc >=2)
{
if((argv[1][0] == '0') && (toupper(argv[1][1]) == 'X'))
{
sscanf(argv[1],"%#X",&port);
}
else
{
cout << "\nUsage: onestep [port]\n";
cout << "Where [port] is an optional argument, of form 0x????,
specifying the port to use.\n";
cout << "If omitted, defaults to 0x378\n\n";
}
}

if(LoadIODLL() != 0)
{
MessageBox(0,"Could not load IODLL", "ERROR", MB_OK);
throw "Could not load IODLL";
}

//don't assume that the port is in a sensible state to start with
PortOut(port,SIG_LOW);

//wait for some milliseconds ... note that seeing as we use sleep,
//this will not be exact!!
Sleep(LOW_TIME_1);

PortOut(port, SIG_HIGH);

Sleep(HIGH_TIME);

PortOut(port, SIG_LOW);

Sleep(LOW_TIME_2);

return 0;
```

D Visual Basic script for Axiovision support of the tomograph

```
Attribute VB_Name = "Axialtomographie"
Public step, StepsBtwStacks, NrOfImageStacks, Visible As Integer

Sub forward(steps)
For i = 1 To steps
    response = Shell
    ("C:\Program Files\Axial Tomography\Motor\forward", vbHide)
    Start = Timer    ' Set start time.
    Do While Timer < Start + 0.01
        DoEvents    ' Yield to other processes for 0.01 sec.
    Loop
    step = (step + 1) Mod 20
    UserForm1.TextBox1.Text = step
    UserForm1.TextBox2.Text = step * 18
    Next i
End Sub

Public Sub SingleStepForward()
    forward (1)
End Sub

Sub backward(steps)
    For i = 1 To steps
    response = Shell
    ("C:\Program Files\Axial Tomography\Motor\backward", vbHide)
    Start = Timer    ' Set start time.
    Do While Timer < Start + 0.01
        DoEvents    ' Yield to other processes for 0.01 sec.
    Loop
    step = (step - 1) Mod 20
    UserForm1.TextBox1.Text = step
    UserForm1.TextBox2.Text = step * 18
    Next i
```

```
End Sub

Public Sub SingleStepBackward()
    backward (1)
End Sub

Public Sub Tomography()
Attribute Tomography.VB_Description = "Manual rotation"
    Dim response
    If step = "" Then step = 0
    If StepsBtwStacks = "" Then StepsBtwStacks = 1
    If NrOfImageStacks = "0" Then NrOfImageStacks = 1
    Load UserForm1
    UserForm1.Show
End Sub

Sub Microscope()
    ZiApplication.ExecuteCommand ("MultidimensionalAcq")
'   response = ZiCommand.Execute()
    Buttons:=vbInformation)
End Sub

Public Sub getCommands()
Dim Commands As ZiCommands

Set Commands = ZiApplication.Commands
For i = 500 To 600
MsgBox Commands.Item(i)
Next i
End Sub
```

Bibliography

[Abel26] Abel N H (1826) Untersuchung der Functionen zweier unabhängig veränderlicher Graphen x und y, wie f(x,y), welche die Eigenschaft haben, daß f(zf(x,y)) eine symmetrische Function von z, x, and y ist. *J. reine angew. Math.* 1: 11

[Abràmoff] Abràmoff M D, Viergever M A (2002) Computation and Visualization of Three Dimensional Motion in the Orbit. *IEEE Trans Med Imag* 4: 21

[Alberts98] Alberts B, Bray D, Lewis J, Raff M, Roberts K, Watson J D (1998) Molecular Biology of the Cell. *Garland Publishing, New York* 2nd Edition

[BioOnline] Biology Online *www.biology-online.org*

[Bradl92] Bradl J, Hausmann M, Ehemann V, Komitowski D, Cremer C (1992) A tilting device for three-dimensional microscopy: application to in situ imaging of interphase cell nuclei. *Journal of Microscopy* 168(1): 47-57

[Bradl94] Bradl J, Hausmann M, Schneider B, Rinke B, Cremer C (1994) A versatile 4π-tilting device for fluorescence microscopes. *Journal of Microscopy* 176(3): 211-221

[Bradl96a] Bradl J, Rinke B, Schneider B, Hausmann M, Cremer C (1996) Improved resolution in 'practical' light microscopy by means of a glass fibre 2π-tilting device. *SPIE* 2628: 140-146

[Bradl96b] Bradl J, Rinke B, Schneider B, Edelmann P, Krieger H, Hausmann M, Cremer C (1996) Resolution improvement in 3-d microscopy by object tilting. *Microscopy and Analysis* 44(11): 9-11

[Carlsson87] Carlsson K, Aslund N (1987) Confocal imaging for 3-D digital microscopy. *Applied Optics* 26: 3232-3238

[Chartrand85] Chartrand G (1985) Introductory Graph Theory. *Dover, New York* p. 116

[Cremer78] Cremer C, Cremer T (1978) Considerations on a laser-scanning-microscope with high resolution and depth of field. *Microscopic Acta (Stuttgart)* 81: 31-44

[Failla03] Failla A V, Albrecht B, Spöri U, Schweitzer A, Kroll A, Bach M, Cremer C (2003) Nanotopology analysis using spatially modulated illumination (SMI) microscopy. *ComPlexUs* 1: 77

[Frank92] Frank J (1992) Electron tomography three-dimensional imaging with the transmission electron microscope. *Plenum, New York*

[Heintzmann99] Heinzmann R (1999) Resolution Enhancement of Biological Light Microscopic Data. *University of Heidelberg* PhD Thesis

[Hell93] Hell S W, Reiner G, Cremer C, Stelzer E H K (1993) Abberations in confocal fluorescence microscopy induced by mismatch in refractive index. *Journal of Microscopy* 169: 391-405

[Holmes94] Holmes T J, Bhattacharyya S, Cooper J, Hanzel D, Krishnamurthi V, Lin W, Roysam B, Szarowski D, Turner J (1994) Blind deconvolution in widefield fluorescence, confocal fluorescence and transmitted brightfield microscopy. *In Programme and Book of Abstracts. Confocal and Near-field Microscopy, 3-D Image Processing in Microscopy*

[Holmes95] Holmes T J, Bhattacharyya S, Cooper J A, Hanzel D, Krishnamurthi V, Lin W, Roysam B., Szarowski D H, Turner J N (1995) Light Microscopic Images Reconstructed by Maximum Likelihood Deconvolution. In James B. Pawley [Ed.], Handbook of Biological Confocal Microscopy. *Plenum Press, New York* 2nd edition, chapter 24.

[Hounsfield73] Hounsfield G N (1973) Computerised transverse axial scanning (tomography) I. Description of system. *British Journal of Radiol* 46: 1016-1022

[Hopkins00] The Johns Hopkins Magazine (2000) *The Johns Hopkins University*

[Jähne99] Jähne B (1999) Handbook of Computer Vision and Applications. *Academic Press* 1st edition, ISBN 0-12-379770-5

[Kempen97] van Kempen G M P, van Vliet L J, Verveer P J, van der Voort H T N (1997) A quantitative comparison of image restoration methods for confocal microscopy. *Journal of Microscopy* 185(3): 354-365

[Kozubek99] Kozubek M, Kozubek S, Lukášová E, Marečková A, Bártová E, Skalníková M, Jergová A (1999) High-resolution cytometry of FISH dots in interphase cell nuclei. *Cytometry* 36: 279-293

[Kozubek01] Kozubek M, Kozubek S, Lukášová E, Bártová E, Skalníková M, Matula P, Matula P, Jirsová P, Cafourková A, Koutná I (2001) Combined confocal and wide-field high-resolution cytometry of fluorescent in situ hybridization-stained cells. *Cytometry* 45: 1-12

[Kozubek02] Kozubek M, Skalníková M, Matula P, Bártová E, Rauch J, Neuhaus F, Eipel H, Hausmann M (2002) Automated micro axial tomography of cell nuclei after specific labelling by fluorescence in situ hybridisation. *Micron* 33: 655-665

[Lewitt86] Lewitt R M, Muehllehner G (1986) Accelerated iterative reconstruction for positron emission tomography based on the EM algorithm for maximum likelyhood estimation. *IEEE Trans Med Imag* 5: 16-22

[Manders93] Manders E M M, Verbeek F J, Aten J A (1993) Measurement of co-localization of objects in dual-colour confocal images. *Journal of Microscopy* 169(3): 375-382

[Manders94] Manders E M M (1994) Dynamics of DNA replication in mammalian cells. *University of Amsterdam* Dissertation

[Markham97] Markham J, Conchello J A (1997) Tradeoffs in regularized maximum-likelihood image restoration. *Proceedings of SPIE* 2984: 136-145

[Minsky61] Minsky M (1961) Microscopy Apparatus. *United States Patent* 3,013,467

[Möbius27] Möbius A F (1827) Der barycentrysche Calcul - ein neues Hülfsmittel zur anaytischen Behandlung der Geometrie. *J.A. Barth, Leipzig*

[Nederlof89] Nederlof P M, Robinson D, Abuknesha R, Wiegant J, Hopman AH, Tanke HJ, Raap AK (1989) Three-color fluorescence in situ hybridization for the simultaneous detection of multiple nucleic acid sequences. *Cytometry* 10: 20-27.

[Neuhaus98] Neuhaus F (1998) Automatisierung der Aufnahme axialtomographischer Bildfolgen an einem Fluoreszenzmikroskop. *University of Heidelberg* Diploma thesis

[Nyquist28] Nyquist H (1928) Certain topics in telegraph transmission theory. *Trans. Amer. Inst. Elect. Eng.* 47: 617

[Olympus] Olympus confocal microscopes *www.olympusconfocal.com*

[Patterson97] Patterson G H, Knobel S M, Sharif W D, Kain S R, Piston D W (1997) Use of the Green Fluorescent Protein and Its Mutants in Quantitative Fluorescence Microscopy. *Biophysical Journal* 73: 2782-2790

[Radon17] Radon J (1917). Über die bestimmung von funktionen durch ihre integralwerte längs gewisser mannigfaltigkeiten. *Ber. Verh. Sachs. Akad. Wiss. Leipzig. Math. Nat. K.* 69:262-277

[Reinhard04] Reinhard B (2004) Überprüfung der thermischen Stabilität von Mikroskopen. *University of Heidelberg* Miniforschung

[Richardson72] Richardson W H (1972) Bayesian-Based Iterative Method of Image Restoration. *Journal of the Optical Society of America* 62(1): 55-59

[Schaefer97] Schaefer L (1997) Increased Spatial Resolution by Using Advanced Restoration Methods for Microscopical Datasets. *Bulletin of the Microscopical Society of Canada* 25(3): 19-25

[Shaw89] Shaw P J, Agard D A, Hirakoa Y, Sedat J W (1989) Tilted view reconstruction in optical microscopy: three dimensional reconstruction of drosophila melanogaster embryo nuclei. *Biophysical Journal* 55: 101-110

[Shaw90] Shaw P J (1990) Three-dimensional optical microscopy using tilted views. *Journal of Microscopy* 158: 165-172

[Silver95] Silver L M (1995) Mouse Genetics Concepts and Applications. *Oxford University Press*

[Slavik96] Slavik J (1996) Fluorescence Microscopy and Fluorescent Probes. *Plenum Press, New York*

[Skaer75] Skaer R J, Whytock S (1975) Interpretation of the three-dimensional structure of living nuclei by specimen tilt. *Journal of Cell Science* 19: 1-10

[Staier02] Staier F (2002) Zellpräparation auf Glasfasern für Distanzmessungen mit dem Mikrotomographen. *University of Heidelberg* Miniforschung

[SVI] Scientific Volume Imaging *www.svi.nl*

[TNHM] The National Health Museum *www.accessexcellence.org*

[Vysis05] *Vysis* http://www.vysis.com

Published parts of this thesis

[Eipel05] Eipel H, Staier F, Cremer C, Matula P, Kozubek M, Hausmann M (2005) Micro Axial Tomography: a miniaturized stage device to overcome resolution anisotropy in fluorescence light microscopy. *Review of Scientific Instruments* (in Preparation)

[Kryvanos05] Kryvanos A, Hesser J, Steidl G (2005) Nonlinear image restoration methods for marker extraction in 3D fluorescent microscopy. *Proceedings of SPIE* 5674: 432-443[1]

[Matula03] Matula P, Kozubek M, Staier F, Hausmann M (2003) Precise 3D image alignment in micro axial tomography. *Journal of Microscopy* 209: 126-142

[1] Contains some microtomographic data of fluorescent beads (chapter 6.2).

Acknowledgment

I thank Prof. Dr. Dr. Christoph Cremer for the supervision of this thesis. In very fruitful discussions he suggested many interesting points and perspectives. Prof. Dr. Michael Hausmann supplied many fruitful ideas. I am very thankful that he always helped me to find a straightforward path of studies.

I am also thankful to Dipl. Ing. Heinz Eipel and Dr. Jutta Finsterle who supported my research with useful discussions and practical help. David Baddeley, Zuhal Kaya, Dr. Nick Kepper, Dr. Gregor Kreth, Helmut Schneider, Dr. Andreas Schweitzer, Dr. Udo Spöri and Dr. Christian Wagner were also very helpful in the clarification of scientific questions. Margund Bach and Rosemarie Eidsness helped me with all kinds of administrative problems. Prof. Dr. Jerzy Doliwa-Dobrucki provided the GFP stained HeLa cells used in this thesis, Dr. Hans van der Voort provided a testing license for the Huygens software package. I am also grateful to the mechanical workshop of the Kirchhoff-Institute, which build the tomograph hardware.

In the Czech Republic I would like to thank Prof. Dr. Stanislav Kozubek and Prof. Dr. Michael Kozubek for very fruitful discussions. They, as well as Dr. Petr Matula, introduced me to automated image analysis.

At Bar Harbor Prof. Dr. Barbara Knowles, Prof. Dr. Lindsay Shopland supported me a lot with fruitful discussions and practical help before and during my stay at the Jackson Lab. Dr. Alexei Evsikov provided lots of good ideas as well as the mouse embryos and oocytes.

Last, not least I would like to thank my parents who supported me in many ways during this thesis.